



1 **Global methane budget and trend, 2010-2017: complementarity of inverse analyses**  
2 **using in situ (GLOBALVIEWplus CH<sub>4</sub> ObsPack) and satellite (GOSAT) observations**

3

4 Xiao Lu<sup>1</sup>, Daniel J. Jacob<sup>1</sup>, Yuzhong Zhang<sup>1,2,3</sup>, Joannes D. Maasakkers<sup>4</sup>, Melissa P. Sulprizio<sup>1</sup>, Lu Shen<sup>1</sup>,  
5 Zhen Qu<sup>1</sup>, Tia R. Scarpelli<sup>1</sup>, Hannah Nesser<sup>1</sup>, Robert M. Yantosca<sup>1</sup>, Jianxiong Sheng<sup>5</sup>, Arlyn Andrews<sup>6</sup>,  
6 Robert J. Parker<sup>7,8</sup>, Hartmut Boech<sup>7,8</sup>, A. Anthony Bloom<sup>9</sup>, Shuang Ma<sup>9</sup>

7

8 <sup>1</sup>John A. Paulson School of Engineering and Applied Sciences, Harvard University, Cambridge, MA,  
9 USA

10 <sup>2</sup>School of Engineering, Westlake University, Hangzhou, Zhejiang Province, China

11 <sup>3</sup>Institute of Advanced Technology, Westlake Institute for Advanced Study, Hangzhou, Zhejiang Province,  
12 China

13 <sup>4</sup>SRON Netherlands Institute for Space Research, Utrecht, The Netherlands.

14 <sup>5</sup>Center for Global Change Science, Massachusetts Institute of Technology, Cambridge, MA, USA

15 <sup>6</sup>National Oceanic and Atmospheric Administration, Earth System Research Laboratory, Boulder, CO,  
16 USA

17 <sup>7</sup>National Centre for Earth Observation, University of Leicester, UK

18 <sup>8</sup>Earth Observation Science, Department of Physics and Astronomy, University of Leicester, UK

19 <sup>9</sup>Jet Propulsion Laboratory, California Institute of Technology, Pasadena, CA, USA

20

21 *Correspondence to:* Xiao Lu (xiaolu@g.harvard.edu) and Yuzhong Zhang

22 (zhangyuzhong@westlake.edu.cn)

23



24 **Abstract**

25 We use satellite (GOSAT) and in situ (GLOBALVIEWplus CH4 ObsPack) observations of atmospheric  
26 methane in a joint global inversion of methane sources, sinks, and trends for the 2010-2017 period. The  
27 inversion is done by analytical solution to the Bayesian optimization problem, yielding closed-form  
28 estimates of information content to assess the consistency and complementarity (or redundancy) of the  
29 satellite and in situ datasets. We find that GOSAT and in situ observations are to a large extent  
30 complementary, with GOSAT providing a stronger overall constraint on the global methane distributions,  
31 but in situ observations being more important for northern mid-latitudes and for relaxing global error  
32 correlations between methane emissions and the main methane sink (oxidation by OH radicals). The  
33 GOSAT observations achieve 212 independent pieces of information (DOFS) for quantifying mean 2010-  
34 2017 anthropogenic emissions on 1009 global model grid elements, and a DOFS of 122 for 2010-2017  
35 emission trends. Adding the in situ data increases the DOFS by about 20-30%, to 262 and 161 respectively  
36 for mean emissions and trends. Our joint inversion finds that oil/gas emissions in the US and Canada are  
37 underestimated relative to the values reported by these countries to the United Nations Framework  
38 Convention on Climate Change (UNFCCC) and used here as prior estimates, while coal emissions in  
39 China are overestimated. Wetland emissions in North America are much lower than in the mean  
40 WetCHARTs inventory used as prior estimate. Oil/gas emissions in the US increase over the 2010-2017  
41 period but decrease in Canada and Europe. Our joint GOSAT+in situ inversion yields a global methane  
42 emission of 551 Tg a<sup>-1</sup> averaged over 2010-2017 and a methane lifetime of 11.2 years against oxidation  
43 by tropospheric OH (86% of the methane sink).

44



## 45 **1 Introduction**

46 Methane (CH<sub>4</sub>) is the second most important anthropogenic greenhouse gas, and plays a central role in  
47 atmospheric chemistry as a precursor of tropospheric ozone and a sink of hydroxyl radicals (OH). It is  
48 emitted from many natural and anthropogenic sources that are difficult to quantify (Saunois et al., 2020).  
49 Atmospheric methane observations from satellites and in situ (surface, tower, shipboard, and aircraft)  
50 platforms have been used extensively to infer methane emissions and their trends through inverse analyses  
51 (Houweling et al., 2017). But the information from satellite and in situ observations does not always agree  
52 (Monteil et al., 2013; Bruhwiler et al., 2017) and is hard to compare because of large differences in  
53 observational density, precision, and the actual quantity being measured (Cressot et al., 2014). Here we  
54 use an analytical solution to the Bayesian inverse problem to quantitatively compare and combine the  
55 information from satellite (GOSAT) and in situ (GLOBALVIEWplus CH<sub>4</sub> ObsPack) observations for  
56 estimating global methane sources and their trends over the 2010-2017 period, including contributions  
57 from different source sectors and from the methane sink (oxidation by tropospheric OH).

58  
59 Inverse analyses of atmospheric methane observations using chemical transport models (CTM) provide a  
60 formal method for inferring methane emissions and their trends (Brasseur and Jacob, 2017). Global  
61 satellite observations of atmospheric methane columns from the shortwave infrared SCIAMACHY and  
62 GOSAT instruments have been widely used for this purpose (Bergamaschi et al., 2013; Wecht et al., 2014;  
63 Turner et al., 2015; Maasakkers et al., 2019; Miller et al., 2019; Lunt et al., 2019). Other inverse analyses  
64 have relied on in situ methane observations that have much higher precision, are more sensitive to surface  
65 emissions, and include isotopic information, but are much sparser (Pison et al., 2009; Bousquet et al., 2011;  
66 Miller et al., 2013; Patra et al., 2016; McNorton et al., 2018).

67  
68 A number of inverse analyses have combined in situ and satellite observations (Bergamaschi et al., 2007,  
69 2009, 2013; Fraser et al., 2013; Monteil et al., 2013; Cressot et al., 2014; Houweling et al., 2014; Alexe et  
70 al., 2015; Ganesan et al., 2017; Janardanan et al., 2020), but few of them have compared the information  
71 from the two data streams and then mostly qualitatively. Bergamaschi et al. (2009, 2013), Fraser et al.  
72 (2014), and Alexe et al. (2015) found that surface and satellite methane observations provided consistent  
73 constraints on global methane emissions, but that satellite observations achieved stronger regional  
74 constraints in the tropics. No study to our knowledge has compared the ability of satellite and in situ  
75 observations to attribute long-term methane trends.

76  
77 Analytical solution to the inverse problem, as used here, provides closed-form error characterization as  
78 part of the solution, and from there allows derivation of the information content from different  
79 components of the observing system (Rodgers, 2000). Application to satellite observations has been used  
80 to determine where the observations can actually constrain the inverse solution (Turner et al., 2015). The  
81 major obstacle to this analytical solution in the past has been the need to construct the Jacobian matrix  
82 for the CTM forward model, but this is now readily done using massively parallel computing clusters  
83 (Maasakkers et al., 2019). Such a method provides a means to quantify the differences in information



84 content between different data streams (e.g., satellite vs. in situ) and from there to contribute to the design  
85 of a better observing system.

86

87 Here we apply satellite observations of atmospheric methane columns from the GOSAT instrument  
88 together with an extensive global compilation of in situ observations (including surface, tower, shipboard,  
89 and aircraft methane measurements) from the GLOBALVIEWplus CH<sub>4</sub> ObsPack v1.0 data product  
90 (Cooperative Global Atmospheric Data Integration Project, 2019), to quantify the global distribution of  
91 methane emissions, loss from reaction with OH, and related trends for the 2010-2017 period. We use for  
92 this purpose an analytical inversion method that formally characterizes the information content from the  
93 two data streams, whether that information is consistent, and whether it is complementary or redundant  
94 (Rodgers, 2000; Jacob et al., 2016). Our work provides a comprehensive global perspective on the sources  
95 contributing to 2010-2017 methane emissions and trends, as well as a general framework for synthesizing  
96 the information from satellite and in situ observations.

97

## 98 **2 Methods**

99 Figure 1 summarizes the components of our analytical inversion system, which builds on previous  
100 inversions of GOSAT satellite data by Maasackers et al. (2019) and Zhang et al. (2019) but adds the in  
101 situ observations. We apply observations  $y$  from GLOBALVIEWplus observations and/or GOSAT  
102 (Section 2.1), with the GEOS-Chem CTM as forward model (Section 2.3), to optimize the state vector  $x$   
103 of our inverse problem. The state vector has dimension  $n = 3378$  including mean 2010-2017 non-wetland  
104 methane emissions on the GEOS-Chem  $4^\circ \times 5^\circ$  global grid ( $n_1 = 1009$ ), 2010-2017 linear trends for these  
105 emissions on that grid ( $n_2 = 1009$ ), monthly mean wetland methane emissions for individual years in 14  
106 subcontinental regions ( $n_3 = 12 \times 8 \times 14 = 1344$ ), and tropospheric OH concentrations in each hemisphere  
107 for individual years ( $n_4 = 2 \times 8 = 16$ ). Section 2.2 describes the prior state vector estimates ( $x_A$ ) and the  
108 prior error covariance matrix ( $S_A$ ). We derive posterior estimates  $\hat{x}$  of the state vector and the associated  
109 error covariance matrix  $\hat{S}$  by analytical solution to the Bayesian optimization problem (Section 2.4). We  
110 present results from three inversions using in situ observations only (In situ-only inversion), GOSAT  
111 observations only (GOSAT-only inversion), and both GOSAT and in situ observations (GOSAT + in situ  
112 inversion).

113

### 114 **2.1 Methane observations**

115 The GLOBALVIEWplus CH<sub>4</sub> ObsPack v1.0 data product compiled by the National Oceanic and  
116 Atmospheric Administration (NOAA) Global Monitoring Laboratory includes worldwide high-accuracy  
117 measurements of atmospheric methane concentrations from different observational platforms (surface,  
118 tower, shipboard, and aircraft) (Cooperative Global Atmospheric Data Integration Project, 2019). Here  
119 we use the ensemble of GLOBALVIEWplus observations for 2010-2017. For surface and tower  
120 measurements, we use only daytime (10-16 local time) observations and average them to the  
121 corresponding daytime mean values. We exclude outliers at individual sites that depart by more than three  
122 standard deviations from the mean. We obtain in this manner 157054 observation data points for the



123 inversion including 81119 from 103 surface sites, 27433 from 13 towers, 827 from 3 ship cruises, and  
124 47675 from 29 aircraft campaigns. Figure 2a shows the mean methane concentrations in 2010-2017 from  
125 the in situ data. The data are relatively dense in North America and western Europe, with also a few sites  
126 in China, but otherwise mainly measure background concentrations. The number of available surface and  
127 tower observations increases from 10493 in 2010 to 19657 in 2017 with largest changes in Europe and  
128 Canada.

129

130 GOSAT is a nadir-viewing instrument in space since 2009 that measures the backscattered solar radiation  
131 from a sun-synchronous orbit at around 13:00 local time (Butz et al., 2011; Kuze et al., 2016). Observing  
132 pixels are 10-km in diameter and separated by about 250 km along-track and cross-track in normal  
133 observation mode, with higher-density data collected in targeted observation modes. Methane is retrieved  
134 at the 1.65  $\mu\text{m}$  absorption band. We use dry column methane mixing ratios from the University of  
135 Leicester version 9.0 Proxy XCH<sub>4</sub> retrieval (Parker et al., 2020). The retrieval has a single-observation  
136 precision of 13 ppb and a regional bias of 2 ppb (Buchwitz et al., 2015). We use GOSAT data for 2010-  
137 2017 including 1.6 million retrievals over land as shown in Figure 2b. We do not use glint data over the  
138 oceans and data poleward of 60°N because of seasonal bias and the potential for large errors (Maasakkers  
139 et al., 2019).

140

## 141 **2.2 Prior estimates**

142 Table 1 summarizes the prior estimates of the mean 2010-2017 methane emissions used for the state vector,  
143 and Figure 3 shows the spatial patterns. Natural sources include the ensemble mean of the WetCHARTS  
144 inventory version 1.2.1 (Bloom et al., 2017) for wetlands, open fires from the Global Fire Emissions  
145 Database version 4s with seasonal and interannual variability (van der Werf et al., 2017), termites from  
146 Fung et al. (1991), and seeps from Etiope et al. (2019) with global scaling to 2 Tg a<sup>-1</sup> from Hmiel et al.  
147 (2020). The default anthropogenic emissions are from EDGAR v4.3.2 (Janssens-Maenhout et al., 2019),  
148 and are superseded for fugitive fuel emissions (oil, gas, coal) by the Scarpelli et al. (2020) inventory  
149 which spatially allocates national emissions reported by countries to the United Nations Framework  
150 Convention of Climate Change (UNFCCC). US anthropogenic emissions are further superseded by the  
151 gridded version of Inventory of U.S. Greenhouse Gas Emissions and Sinks from the Environmental  
152 Protection Agency (EPA GHGI) (Maasakkers et al., 2016). The WetCHARTS wetlands inventory includes  
153 seasonal and interannual variability that is optimized in the inversion through correction to the monthly  
154 emissions. Seasonality from Zhang et al. (2016) is imposed for rice emissions, and temperature-dependent  
155 seasonality is applied to manure emissions (Maasakkers et al., 2016). Other emissions are aseasonal.

156

157 We assume a 50% error standard deviation for all anthropogenic and non-wetland natural emissions on  
158 the 4° latitude × 5° longitude grid, with no spatial error covariance so that their prior error covariance  
159 matrix is diagonal, which is a reasonable assumption for anthropogenic emissions (Maasakkers et al.,  
160 2016). We assume 0 ± 10% a<sup>-1</sup> as prior estimate for the linear 2010-2017 emission trends on the 4° × 5°  
161 grid. Prior estimates of monthly mean wetland methane emissions for individual years in 14



162 subcontinental regions, along with their error covariance matrix, are from the WetCHART v1.2.1  
163 inventory ensemble (Bloom et al., 2017). The prior methane emissions total  $533 \text{ Tg a}^{-1}$ , at the low end of  
164 the current top-down estimates ( $538\text{--}593 \text{ Tg a}^{-1}$ ) for 2008-2017 (Saunois et al., 2020), and this largely  
165 reflects the downward revision of global seep emissions by Hmiel et al. (2020).

166

167 Prior monthly 3-D fields of global tropospheric OH concentrations are taken from a GEOS-Chem  
168 simulation with full-chemistry (Wecht et al., 2014) that yields a methane lifetime  $\tau_{\text{CH}_4}^{\text{OH}}$  due to oxidation  
169 by tropospheric OH of  $10.6 \pm 1.1$  years and an inter-hemispheric OH ratio (North to South) of 1.16. The  
170 methane lifetime is consistent with the value of  $11.2 \pm 1.3$  years inferred from methylchloroform  
171 observations (Prather et al., 2012), while the inter-hemispheric OH ratio is slightly higher than the  
172 observed range of  $0.97 \pm 0.12$  (Patra et al., 2014) but closed to recent multi-model estimates of  $1.3 \pm 0.1$   
173 (Zhao et al., 2019). We assume no interannual variability in this prior OH field. We use 10% as prior error  
174 standard deviation for the hemispheric OH concentrations in individual years, based on Holmes et al.  
175 (2013). Corrections to OH in the inversion are applied as a hemispheric scaling factor for individual years,  
176 without changing the spatial or temporal pattern of the original fields. Zhang et al. (2018) conducted  
177 methane inversions with twelve different OH fields from the ACCMIP model ensemble (Naik et al., 2013)  
178 and found no significant difference with the GEOS-Chem OH fields used here except for two outlier  
179 models.

180

### 181 2.3 Forward Model

182 We use the GEOS-Chem 12.5.0 (<http://geos-chem.org>) global CTM (Bey et al., 2001; Wecht et al., 2014;  
183 Maasackers et al., 2019) as forward model to simulate atmospheric methane concentrations and their  
184 sensitivity to the state vector elements. The model is driven by MERRA-2 reanalysis meteorological fields  
185 from the NASA Global Modeling and Assimilation Office (GMAO) (Gelaro et al., 2017). The methane  
186 sink is computed within the model from 3-D tropospheric oxidant fields including OH (optimized in the  
187 inversion), Cl atoms (Wang et al., 2019), 2-D stratospheric oxidant fields (Murray et al., 2012), and soil  
188 uptake (Murguia-Flores et al., 2018). We conduct GEOS-Chem model simulations for 2010-2017 at  
189 global  $4^\circ \times 5^\circ$  resolution with 47 vertical layers extending to the mesosphere. GEOS-Chem has excessive  
190 methane in the high-latitudes stratosphere, a flaw common to many models (Patra et al., 2011), and we  
191 correct for this bias, with stratospheric methane profiles measured by the solar occultation ACE-FTS v3.6  
192 instrument (Waymark et al., 2014; Koo et al., 2017) following Zhang et al. (2019). Initial model conditions  
193 on January 1, 2010 are set to be unbiased in zonal mean relative to GOSAT observations for January 2010,  
194 and we find that they are also unbiased relative to the GLOBALVIEWplus in situ observations. In this  
195 manner, model discrepancies with observations over the 2010-2017 period can be attributed to model  
196 errors in emissions or OH over that period, instead of error in initial conditions. We archive model  
197 methane dry mixing ratios at each location and time of the in situ and GOSAT datasets for 2010-2017.

198

199 As forward model  $F$  for the inversion, GEOS-Chem relates the state vector  $\mathbf{x}$  to the atmospheric  
200 concentrations  $\mathbf{y}$  as  $\mathbf{y} = F(\mathbf{x})$  (Fig.1). The simulation of observations with the prior estimates of state



201 vectors ( $\mathbf{x}_A$ ) in 2010-2017 diagnoses systematic errors in comparison to observations that enable  
202 improved estimate of the state vector through the inversion. In addition, the random component of the  
203 discrepancy can be used to estimate the observation error (sum of instrument error, representation error,  
204 and forward model error) in the Bayesian optimization problem using the residual error method (Heald et  
205 al., 2004). The method assumes that the systematic component of the model bias ( $\overline{\mathbf{y} - \mathbf{F}(\mathbf{x}_A)}$ ) for  
206 individual years, where the overbar denotes the temporal average in a  $4^\circ \times 5^\circ$  grid cell (for GOSAT) or for  
207 an observation platform (for in situ observations), is to be corrected in the inversion, while the residual  
208 term ( $\varepsilon_0 = \mathbf{y} - \mathbf{F}(\mathbf{x}_A) - \overline{\mathbf{y} - \mathbf{F}(\mathbf{x}_A)}$ ) represents the random observation error. Here we applied this  
209 method to construct the observation error covariance matrix  $\mathbf{S}_0$  from the statistics of  $\varepsilon_0$ .

210

211 We find that the mean standard deviation of the random observation error ( $\varepsilon_0$ ) for the GLOBALVIEWplus  
212 in situ data averages 36 ppbv (20 and 45 ppbv for background and non-background surface observations,  
213 68 ppbv for tower observations, 10 ppbv for shipboard observations, 24 ppbv for aircraft observations),  
214 compared to 13 ppbv for GOSAT. The observation error for in situ observations is dominated by the  
215 forward model error while for GOSAT it is dominated by the instrument error. The forward model error  
216 is higher for surface concentrations near source regions than for columns or other in situ observations  
217 measuring background, because the amplitude of methane variability is much higher (Cusworth et al.,  
218 2018) and more challenged for a model at  $4^\circ \times 5^\circ$  resolution to capture. We assume that  $\mathbf{S}_0$  is diagonal  
219 in the absence of better objective information, but in fact some error correlation between different  
220 observations could be expected to arise from transport and source aggregation errors in the forward model.  
221 This is considered by introducing a regularization factor  $\gamma$  in the minimization of the cost function for  
222 the inversion (Section 2.4).

223

## 224 2.4 Analytical Inversion

225 Bayesian solution to the state vector optimization problem assuming Gaussian prior and observation  
226 errors involves minimizing the cost function  $J(\mathbf{x})$ :

$$227 \quad J(\mathbf{x}) = (\mathbf{x} - \mathbf{x}_A)^T \mathbf{S}_A^{-1} (\mathbf{x} - \mathbf{x}_A) + \gamma (\mathbf{y} - \mathbf{F}(\mathbf{x}))^T \mathbf{S}_0^{-1} (\mathbf{y} - \mathbf{F}(\mathbf{x})) \quad (1),$$

228 where  $\mathbf{x}$  is the state vector,  $\mathbf{x}_A$  denotes the prior estimate of  $\mathbf{x}$ ,  $\mathbf{S}_A$  is the prior error covariance matrix,  
229  $\mathbf{y}$  is the observation vector,  $\mathbf{F}(\mathbf{x})$  represents the GEOS-Chem simulation of  $\mathbf{y}$ ,  $\mathbf{S}_0$  is the observation  
230 error covariance matrix, and  $\gamma$  is a regularization factor. The need for  $\gamma$  in  $J(\mathbf{x})$  is to avoid giving  
231 excessive weighting to observations, due to the likely underestimate of  $\mathbf{S}_0$  when unknown error  
232 correlations are not included in its construction (Zhang et al., 2018; Maasakkers et al., 2019).  $\gamma$  here plays  
233 the same role as the regularization parameter in Tikhonov methods (Brasseur and Jacob, 2017) and reflects  
234 our inability to properly quantify the magnitude of errors.

235

236 Minimization of the cost function in equation (1) has an analytical solution if the forward model is linear  
237 (Rodgers, 2000). The inverse problem here is not strictly linear regarding the optimization of OH, because  
238 the sensitivity of the methane concentration to change in OH concentrations depends on the methane  
239 concentration through first-order loss. The variability of methane concentration is sufficiently small that



240 this non-linearity is negligible. We thus express the GEOS-Chem forward model as  $\mathbf{y} = \mathbf{K}\mathbf{x} + \mathbf{c}$ , where  
241  $\mathbf{K} = \partial\mathbf{y}/\partial\mathbf{x}$  represents the Jacobian matrix and  $\mathbf{c}$  is an initialization constant. We construct the Jacobian  
242 matrix  $\mathbf{K}$  explicitly by conducting GEOS-Chem simulations with each element of the state vector  
243 perturbed separately. Minimizing the Bayesian cost function by solving  $dJ(\mathbf{x})/d\mathbf{x} = \mathbf{0}$  yields closed-  
244 form expressions for the posterior estimate of the state vector  $\hat{\mathbf{x}}$  and its error covariance matrix  $\hat{\mathbf{S}}$ :

$$245 \quad \hat{\mathbf{x}} = \mathbf{x}_A + \mathbf{G}(\mathbf{y} - \mathbf{K}\mathbf{x}_A) \quad (2),$$

$$246 \quad \hat{\mathbf{S}} = (\gamma\mathbf{K}^T\mathbf{S}_O^{-1}\mathbf{K} + \mathbf{S}_A^{-1})^{-1} \quad (3),$$

247

248 where  $\mathbf{G}$  is the gain matrix,

$$249 \quad \mathbf{G} = \frac{\partial\hat{\mathbf{x}}}{\partial\mathbf{y}} = (\gamma\mathbf{K}^T\mathbf{S}_O^{-1}\mathbf{K} + \mathbf{S}_A^{-1})^{-1}\gamma\mathbf{K}^T\mathbf{S}_O^{-1} \quad (4).$$

250

251 From the posterior error covariance matrix one can derive the averaging kernel matrix describing the  
252 sensitivity of the posterior estimate to the true state:

$$253 \quad \mathbf{A} = \frac{\partial\hat{\mathbf{x}}}{\partial\mathbf{x}} = \mathbf{I}_n - \hat{\mathbf{S}}\mathbf{S}_A^{-1} \quad (5).$$

254 The trace of  $\mathbf{A}$  quantifies the degrees of freedom for signal (DOFS), which represents the number of  
255 pieces of independent information gained from the observing system for constraining the state vector  
256 (Rodgers, 2000).

257

258 We choose the value for the regularization parameter  $\gamma$  in order to achieve a solution most consistent  
259 with the estimated error on the prior estimates. For a given state vector element  $i$ , the expected value of  
260  $(\hat{\mathbf{x}}_i - \mathbf{x}_{Ai})^2$  is the prior error variance  $\sigma_{Ai}^2$ . For a diagonal prior error covariance matrix, the state  
261 component  $J_A$  of the posterior cost function is

$$262 \quad J_A(\hat{\mathbf{x}}) = (\hat{\mathbf{x}} - \mathbf{x}_A)^T\mathbf{S}_A^{-1}(\hat{\mathbf{x}} - \mathbf{x}_A) = \sum_n \frac{(\hat{\mathbf{x}}_i - \mathbf{x}_{Ai})^2}{\sigma_{Ai}^2} \approx n \quad (6),$$

263

264 where  $n$  is the number of state vector elements. In our case the prior error covariance matrix is not strictly  
265 diagonal because of covariance for the wetland terms (Bloom et al., 2017), so one may expect  $J_A(\hat{\mathbf{x}})$  to  
266 be somewhat deviated from  $n$ . Nevertheless,  $J_A(\hat{\mathbf{x}}) \gg n$  implies overfit to the observations because the  
267 posterior state vector estimates are far outside the estimated errors on the prior estimates.

268

269 One can apply the same reasoning to the observation component  $J_O$  of the posterior cost function,

$$270 \quad J_O(\hat{\mathbf{x}}) = (\mathbf{y} - \mathbf{K}\hat{\mathbf{x}})^T\mathbf{S}_O^{-1}(\mathbf{y} - \mathbf{K}\hat{\mathbf{x}}) \approx m \quad (7),$$

271

272 where  $m$  is the number of observations. However, this component is less sensitive to the choice of  $\gamma$   
273 because of the large random error component for individual observations.

274

275 Figure 4 shows the dependences of  $J_A(\hat{\mathbf{x}})$  and  $J_O(\hat{\mathbf{x}})$  on the choice of the regularization parameter  $\gamma$ , for  
276 the in situ and GOSAT observations. The in situ observations are sufficiently sparse that  $\gamma = 1$  (no



277 regularization) provides the best solution. In the case of GOSAT, however,  $\gamma = 1$  would yield  $J_A(\hat{\mathbf{x}}) = 6n$   
278 which indicates overfit, while  $\gamma = 0.1$  yields  $J_A(\hat{\mathbf{x}}) \approx n$  which is the expected value and is used here.  
279 This can be explained by the high observation density of GOSAT, such that error correlation between  
280 individual observations may be expected and would have a large effect on the solution. Maasakkers et al.  
281 (2019) found that  $\gamma = 0.05$  and  $\gamma = 0.1$  gave similar solutions in their global inversions of GOSAT  
282 data.

283

284 Analytical solution to the cost function minimization problem, as done here, has several advantages  
285 relative to the more commonly used variational (numerical) approach for finding the minimum. (1) It  
286 finds the true minimum in the cost function, rather than an approximation that may be sensitive to the  
287 choice of initial estimate. (2) It identifies the information content of the inversion and the ability to  
288 constrain each state vector element. (3) It enables a range of sensitivity analyses modifying the prior  
289 estimates, modifying the error covariance matrices, adding/subtracting observations, etc. at minimal  
290 computational cost. We will make use of these advantages in comparing the ability of the In situ-only,  
291 GOSAT-only, and GOSAT + in situ inversions. A requirement of the analytical approach is that the  
292 Jacobian matrix be explicitly constructed, requiring  $n + 1$  forward model runs. However, this construction  
293 is readily done in parallel on high-performance computing clusters.

294

295 Our inversion returns posterior emission estimates and their temporal trends on a  $4^\circ \times 5^\circ$  grid for non-  
296 wetland emissions, and monthly mean wetland emissions for individual years in 14 subcontinental regions.  
297 We can aggregate these results spatially and by sector in a way that retains the error covariance of the  
298 solution (Maasakkers et al., 2019). Consider a reduced state vector  $\mathbf{x}_{red}$  representing a linear combination  
299 of the original state vector elements that may be a sum over a particular region or the globe, and may be  
300 weighted by the contributions from individual sectors following the prior distribution. The linear  
301 transformation from the posterior full-dimension state vector  $\hat{\mathbf{x}}$  to the reduced state vector  $\hat{\mathbf{x}}_{red}$  is  
302 defined by a summation matrix  $\mathbf{W}$

303

$$\hat{\mathbf{x}}_{red} = \mathbf{W}\hat{\mathbf{x}} \quad (8).$$

304

305 The posterior error covariance and averaging kernel matrices for the reduced state vector can then be  
306 calculated as:

307

$$\hat{\mathbf{S}}_{red} = \mathbf{W}\hat{\mathbf{S}}\mathbf{W}^T \quad (9),$$

308

$$\mathbf{A}_{red} = \mathbf{W}\mathbf{A}\mathbf{W}^* \quad (10),$$

309

310 where  $\mathbf{W}^* = \mathbf{W}^T(\mathbf{W}\mathbf{W}^T)^{-1}$  (Calisesi et al., 2005).  $\hat{\mathbf{S}}_{red}$  provides a means to determine error  
311 correlations between aggregates of quantities optimized by the inversion, e.g., between global methane  
312 emissions and global OH concentrations.  $\mathbf{A}_{red}$  provides a means to determine the ability of the inversion  
313 to constrain an aggregated term (e.g., emissions from a particular sector).

313

### 314 3. Results and discussion

#### 315 3.1 Ability to fit the in situ and GOSAT data



316 We will present results from three different inversions for 2010-2017: (1) using only in situ observations  
317 (In situ-only inversion), (2) using only GOSAT observations (GOSAT-only inversion), and (3) using both  
318 GOSAT and in situ observations (GOSAT + in situ inversion). Here we first evaluate the ability of these  
319 different inversions to fit the in situ and GOSAT observations, including when the data are not used in the  
320 inversion (consistency check). This is done by conducting GEOS-Chem simulations with posterior values  
321 for the state vectors and comparing to observations.

322

323 Figures 5 and 6 show the resulting comparisons for the in situ observations, arranged by type of platform  
324 (Fig.5), and by latitude bands and months (panels (a)-(d) in Fig.6). The model simulation with prior  
325 estimates shows a 30-60 ppb low bias for all in situ platforms growing with time. The In situ-only  
326 inversion effectively corrects this bias and its trend, and also significantly improves the correlations across  
327 all platforms. The GOSAT-only inversion performs comparably in correcting the bias for the independent  
328 aircraft data measuring the background, and also corrects the 2010-2017 trend, but still shows notable  
329 low bias at northern mid-latitudes because of difficulty in fitting the surface and tower data in the US and  
330 Europe that are adjacent to methane sources.

331

332 Figure 6 also compares the fits to the GOSAT observations (panels (e)-(h)). Both the In situ-only and  
333 GOSAT-only inversions correct the bias and trend in the prior simulation at all latitudes. An important  
334 implication is that the in situ observations, even though sparse and mostly at northern mid-latitudes, can  
335 still inform the global methane levels. The GOSAT + in situ joint inversion shows good agreement with  
336 both the in situ and GOSAT observations.

337

338 Figure 7 further evaluates the global methane growth rate as determined by the methane budget imbalance  
339 for individual year in 2010-2017 from the three inversions. The observed methane growth rate inferred  
340 from the NOAA sites ([https://www.esrl.noaa.gov/gmd/ccgg/trends\\_ch4/](https://www.esrl.noaa.gov/gmd/ccgg/trends_ch4/), last access: 20 June 2020)  
341 averages  $7.2 \pm 2.8$  ppb  $a^{-1}$  over the period, peaking in 2014, and overall accelerating with higher growth in  
342 2015-2017 than in 2010-2013. We find that all posterior simulations show comparable mean methane  
343 growth rate ( $7.7 \pm 3.7$  ppb  $a^{-1}$  for In situ-only inversion,  $8.8 \pm 2.2$  ppb  $a^{-1}$  for GOSAT-only inversion, and  
344  $8.3 \pm 1.8$  ppb  $a^{-1}$  for the GOSAT + in situ inversion). However, the In situ-only inversion overestimates the  
345 increasing trend in the methane growth rate, largely driven by year 2017, and fails to fit its interannual  
346 variability. This may reflect the heavy weighting of the in situ observations toward northern mid-latitudes.  
347 GOSAT observations in the inversion do much better in capturing the observed methane interannual  
348 variability and trend. Adding in situ observations to GOSAT observations provides a better fit in 2015  
349 than GOSAT-only inversion but has insignificant effect in other years. Zhang et al. (2019) interpreted the  
350 trend and interannual variability in the GOSAT-only inversion as due to a combination of anthropogenic  
351 emissions, wetlands, and OH concentrations.

352

### 353 **3.2 Anthropogenic methane emissions**

354 Figure 8 shows the averaging kernel sensitivities (diagonal elements of the averaging kernel matrix) and



355 posterior scaling factors for the non-wetland emissions (dominated by anthropogenic emissions) in the In  
356 situ-only, GOSAT-only, and GOSAT + in situ joint inversions. The DOFS (trace of the averaging kernel  
357 matrix) quantify the number of independent pieces of information from the inversion, starting from 1009  
358 unknowns for anthropogenic emissions (Figure 1). The DOFS are 113 for the In situ-only inversion, 212  
359 for the GOSAT-only inversion, and 262 for the GOSAT + in situ joint inversion. The higher DOFS from  
360 the joint inversion indicate that the satellite and in situ observations have complementarity but also some  
361 redundancy. Strict complementarity would imply a DOFS of  $325=113+212$ . We find that 75% of the in  
362 situ information is at northern mid-latitudes ( $30-60^{\circ}\text{N}$ , DOFS=82, calculated as the sum of averaging  
363 kernel sensitivities in that latitude band) where the observations are densest, with another 9% (DOFS=10)  
364 at  $60-90^{\circ}\text{N}$ . GOSAT provides higher information than in situ observations at northern mid-latitudes  
365 (DOFS=96) and dominates in the tropics (DOFS=105). This dominance of satellites for informing  
366 methane sources in the tropics has been pointed out in previous studies (Bergamaschi et al., 2013; Monteil  
367 et al., 2013; Fraser et al., 2013; Alexe et al., 2015).

368

369 We investigate further the inversion results for northern mid-latitudes where most of the information of  
370 in situ observations is contained including for the US, Canada, Europe, and China. Table 2 gives the  
371 optimization of anthropogenic methane emissions (calculated as the difference between total non-wetland  
372 emissions and the non-wetland natural emissions) in these regions. Figure 9 shows the optimization by  
373 source sectors, assuming that (1) the partitioning between sectors of non-wetland emissions in individual  
374 grid cells is correct in the prior inventory (this does not assume that the prior distribution of sectoral  
375 emissions is correct), (2) the scaling factors are to be applied equally to all sectors in a grid cell. These  
376 assumptions are adequate when the sectors are spatially separated but are more prone to error when they  
377 spatially overlap. Figure 9 also shows the averaging kernel sensitivities of emission sectors (diagonal  
378 terms of  $A_{red}$  derived from Equations (8) and (10)), measuring the ability of the inversion to optimize  
379 different emissions sectors, and the DOFS for each inversion summed over the region. Wetland methane  
380 emissions are optimized separately as will be discussed in Section 3.3.

381

382 Inspection of the DOFS shows that the in situ observations are more effective than GOSAT for optimizing  
383 US anthropogenic methane emissions (DOFS=41 vs. DOFS=22) and this applies to all sectors (Figure 9).  
384 The averaging kernel sensitivities panel in Figure 9 shows that US results from the joint GOSAT + in situ  
385 inversion are mostly determined by the in situ observations. The joint GOSAT + in situ inversion increases  
386 anthropogenic US emissions from  $28 \text{ Tg a}^{-1}$  in the prior EPA GHGI to  $36 \text{ Tg a}^{-1}$ , with most of the increase  
387 driven by livestock and oil/gas sources in the central US. Averaging kernel sensitivity for major sectors  
388 is large (0.63-0.93), indicating that the posterior estimates are mostly determined by the observations  
389 rather than by the prior estimates. The underestimate of oil/gas emissions in the EPA GHGI has been  
390 reported before (Alvarez et al., 2018; Cui et al., 2019; Maasakkers et al., 2020).

391

392 In situ observation is also more effective than GOSAT in optimizing anthropogenic methane emissions in  
393 Canada (DOFS=21 vs. DOFS=6), particularly in Alberta where oil/gas emissions are high (Fig.8). This



394 reflects in part our exclusion of GOSAT data poleward of 60°N. Oil/gas emissions in Canada increase by  
395 a factor of 2 in the GOSAT + in situ inversion to 4.5 Tg a<sup>-1</sup> compared to the ICF (2015) prior estimate,  
396 with an averaging kernel sensitivity of 0.57 (Fig.9). Total anthropogenic emissions increase from 5 Tg a<sup>-1</sup>  
397 to 8 Tg a<sup>-1</sup>.

398

399 In situ and GOSAT observations show comparable ability in optimizing the total anthropogenic emissions  
400 in Europe (DOFS=16~18). They agree that prior anthropogenic methane emissions are too high in  
401 northern Europe but disagree in southern Europe. Averaging kernel sensitivities from the In situ-only  
402 inversion are slightly weaker than for the US and Canada because of the lower density of in situ sites. The  
403 Integrated Carbon Observation system (ICOS) network (<https://www.icos-cp.eu/>, last access: 17 July  
404 2020) has increased substantially the number of available methane observations in Europe since 2017 so  
405 that future inversions should expect a stronger constraint from in situ observations. Total European  
406 anthropogenic emissions decrease from 27 Tg a<sup>-1</sup> to 23 Tg a<sup>-1</sup> in the GOSAT + in situ joint inversion, with  
407 decreases for all sectors but this may reflect the inability of our 4°× 5° resolution to effectively separate  
408 emission sectors.

409

410 The only other region where in situ observation provides significant information is China, though the  
411 corresponding DOFS=13 is less than for GOSAT (DOFS=22). Both inversions agree that emissions must  
412 be greatly decreased from the prior estimate, and the joint inversion (DOFS=28) has stronger power in  
413 doing so. The posterior 2010-2017 Chinese anthropogenic emission is 43 Tg a<sup>-1</sup> in the joint inversion,  
414 compared to 63 Tg a<sup>-1</sup> in the prior estimate. Our results agree with a recent study by Janardanan et al.  
415 (2020), which also used GOSAT and surface observations to estimate a mean 2011-2017 anthropogenic  
416 methane emission in China of 46±9 Tg a<sup>-1</sup>. The downward correction is mainly driven by a 40% decrease  
417 in coal emissions from 19 Tg a<sup>-1</sup> to 11 Tg a<sup>-1</sup> (Fig. 9). Previous inversions using the EDGAR inventory  
418 (>20 Tg a<sup>-1</sup>) as prior estimate found a similar correction (Alexe et al., 2015; Thompson et al., 2015; Turner  
419 et al., 2015; Maasackers et al., 2019; Miller et al., 2019). In our case, the prior estimate of coal emissions  
420 (19 Tg a<sup>-1</sup>) is the value reported by China to the UNFCCC and we find that it is still too high. A recent  
421 inventory by Sheng et al. (2019) gives a coal emission estimate of 15 Tg a<sup>-1</sup> for China in 2010-2016.

422

### 423 3.3 Wetland methane emissions

424 The inversion optimizes wetland emissions for the 14 regions of Figure 3 and for 96 individual months  
425 covering 2010-2017, amounting to 1344 state vector elements. Results from the In situ-only, GOSAT-  
426 only, and GOSAT + in situ inversions yield DOFS of 221, 183, and 301 respectively. In situ observations  
427 provide more information for boreal wetlands while GOSAT dominates for tropical wetlands.

428

429 We analyzed further the boreal/temperate North America wetlands, where in situ observations provide  
430 significant added information (Figure 10). Both in situ and GOSAT observations agree that the prior  
431 WetCHARTs emissions are too high. The posterior estimates from the GOSAT + in situ inversion are 4.5  
432 and 2.0 Tg a<sup>-1</sup> for boreal and temperate North America, respectively, compared to 12.8 and 6.9 Tg a<sup>-1</sup> in



433 WetCHARTs. Posterior boreal wetland CH<sub>4</sub> emissions are on the lower end but within the WetCHARTs  
434 estimates (WetCHARTs models range 3~33 Tg a<sup>-1</sup>); however, posterior temperate CH<sub>4</sub> emissions are  
435 lower and outside WetCHARTs range (3~12 Tg a<sup>-1</sup>). The correction for boreal North America is  
436 particularly large in May-June, which can potentially be attributed to suppression of wetland emissions  
437 by either snow cover (Pickett-Heaps et al., 2011) or by frozen soils (Zona et al., 2016). The WetCHARTs  
438 emission overestimate for temperate North America (mainly coastal wetlands in the eastern US) has been  
439 reported before from inversions using aircraft data (Sheng et al., 2018) and GOSAT data (Maasakkers et  
440 al., 2020).

441

### 442 **3.4 Anthropogenic methane emission trends**

443 Figure 11 presents the 2010-2017 trends of anthropogenic methane emissions from the three inversions,  
444 and the corresponding averaging kernel sensitivities. The GOSAT + in situ inversion has a DOFS = 161  
445 for quantifying the spatial distribution of the trends. Most of that information is from GOSAT (DOFS =  
446 122) but in situ observations add significant information. Information from in situ observations is  
447 concentrated in the US, Canada, Europe, and China. Table 2 summarizes the trends for the four regions.  
448 Figure 12 shows the trends disaggregated by sectors, using the same procedure as for Figure 9.

449

450 In situ observations provide stronger constraints than GOSAT on anthropogenic emission trends in the  
451 US (DOFS=29 vs. DOFS=12). They agree on the upward trend in the eastern US as also found in  
452 Maasakkers et al. (2020) which used GOSAT in a high resolution inversion to interpret methane trends in  
453 US in 2010-2015. However, they show opposite trends (positive trend from In situ-only inversion but  
454 negative from GOSAT-only inversion) in total emissions and in the central south US (Table 2, Fig. 11).  
455 The GOSAT + in situ joint inversion (DOFS=31) estimates that US anthropogenic methane emissions  
456 increased by 0.4 Tg a<sup>-1</sup> a<sup>-1</sup> (1.1% a<sup>-1</sup>) from 2010 to 2017, with the largest contribution from oil/gas  
457 emissions (0.3 Tg a<sup>-1</sup> a<sup>-1</sup>, 2.5% a<sup>-1</sup>). This posterior trend is much smaller than previous studies showing  
458 large increases in US oil/gas emissions (2.1–4.4 Tg a<sup>-1</sup> a<sup>-1</sup>) inferred from ethane/propane levels (Franco  
459 et al., 2016; Hausmann et al., 2016; Helmig et al., 2016), but is more consistent with a recent study by  
460 Lan et al. (2019) of 0.3±0.1 Tg a<sup>-1</sup> a<sup>-1</sup> in 2006-2015 based on long-term in situ measurements. The  
461 inversion also reveals rising emissions from oil/gas in the central south US, including the Permian Basin  
462 which is currently the largest oil-producing basin in the US (Zhang et al., 2020).

463

464 We find that anthropogenic emissions in Canada decrease over the 2010-2017 period by 0.2 Tg a<sup>-1</sup> a<sup>-1</sup>  
465 (2.5% a<sup>-1</sup>) in the GOSAT + in situ joint inversion, mostly driven by oil/gas emissions in Alberta and  
466 livestock emissions (Figs. 11-12). Anthropogenic emissions in Europe decrease by 0.4 Tg a<sup>-1</sup> a<sup>-1</sup> (1.7 % a<sup>-1</sup>).  
467

468

469 All three inversions show increases of Chinese anthropogenic methane emissions over 2010-2017 by 0.1-  
470 0.4 Tg a<sup>-1</sup> a<sup>-1</sup> (0.3-0.9% a<sup>-1</sup>), but the spatial patterns and source attributions are different. The largest  
471 difference is for coal mining emissions in the North China Plain, where in situ observations indicates a



472 decrease by  $-0.8 \text{ Tg a}^{-1} \text{ a}^{-1}$  while GOSAT shows an increase by  $0.1 \text{ Tg a}^{-1} \text{ a}^{-1}$ . A previous GOSAT inversion  
473 study found a large increase of coal mining emissions in China over 2010-2015 (Miller et al., 2019).  
474 However, a recent bottom-up inventory estimates that Chinese coal emission peaked in 2012 and  
475 decreased afterward, leading to no significant overall trend for 2010-2016 (Sheng et al., 2019). Our  
476 inversion assumes linear trends in emissions over 2010-2017 but that may not be appropriate for China.  
477

### 478 **3.5 Global methane budget for 2010-2017**

479 Table 1 shows the optimized global anthropogenic emissions from different sectors as determined by the  
480 joint GOSAT + in situ inversion. Corrections to the global prior estimates are mostly determined by  
481 GOSAT (Fig. 8). They include upward corrections to livestock and rice methane emissions, and  
482 downward correction to the coal mining emissions driven by overestimation in China. The joint inversion  
483 also estimates a global increase in anthropogenic emissions by  $1.7 \pm 0.6 \text{ Tg a}^{-1} \text{ a}^{-1}$  ( $0.5\% \text{ a}^{-1}$ ) in 2010-2017,  
484 dominantly driven by trends in the tropics (Fig. 11).  
485

486 A number of previous studies have analyzed surface observations to interpret global methane budgets and  
487 trends (Dlugokencky et al., 2009; Bruhwiler et al., 2014; Houweling et al., 2017). As shown in Figure 6,  
488 our In situ-only inversion can fit the GOSAT observations of global methane distribution and trend,  
489 indicating that the in situ data provide useful information on the global budget. Here we examine whether  
490 this information adds to that from GOSAT. For this purpose and following Maasackers et al. (2019), we  
491 collapse the full state vector to a reduced state vector ( $\hat{\mathbf{x}}_{red}$ ) that contains global mean methane emissions  
492 and OH as elements, and derive the associated error covariance matrix ( $\hat{\mathbf{S}}_{red}$ ) as introduced in Section  
493 2.4.  
494

495 Figure 13 shows the joint probability density functions (PDFs) of the mean anthropogenic methane  
496 emissions and methane lifetime against oxidation by tropospheric OH from the three inversions. There is  
497 strong negative correlation ( $r=-0.72$ ) between the optimization of methane emissions and OH in the  
498 GOSAT-only inversion, and somewhat less in the In situ-only inversion ( $r=-0.53$ ), although the posterior  
499 error variance is larger due to the lower data density as indicated by the axes of the ellipses. A sensitivity  
500 inversion using only the surface and tower measurements in the In situ-only inversion yields  $r=-0.36$ . It  
501 indicates that in situ observations are more effective than the satellite observations in independently  
502 constraining methane emissions from the sink by OH. A likely reason is that surface measurements in  
503 source regions are more sensitive to methane emissions than are column measurements.  
504

505 Comparison of the posterior PDFs between the GOSAT-only and In situ-only inversions implies that the  
506 two are inconsistent, since the 99% probability contour does not overlap (Fig.13), but this is likely because  
507 the posterior error covariance matrix underestimates the actual error variance in particular for global  
508 budget errors due to its assumption of independent identically distributed (IID) observational errors  
509 (Brasseur and Jacob, 2017). Remarkably, the GOSAT + in situ joint inversion is more in agreement with  
510 in situ observations than GOSAT. Inspection of Figure 6c shows that the GOSAT-only inversion is biased



511 low relative to in situ observations at northern mid-latitudes and biased high in the southern hemisphere,  
512 implying that both emissions and OH concentrations are too low. Ingestion of the in situ observations in  
513 the inversion corrects that bias, and narrows the posterior error of mean anthropogenic emissions and  
514 methane lifetime against tropospheric OH by 30% (Fig. 13), compared to the GOSAT-only inversion.  
515 Thus we find that the GOSAT and in situ observations are complementary in quantifying the global budget.

516  
517 Table 3 summarizes the global mean methane budget in 2010-2017. The GOSAT + in situ joint inversion  
518 estimates a total methane emission of  $551 \pm 2$  Tg  $\text{a}^{-1}$ , of which 371 Tg  $\text{a}^{-1}$  are anthropogenic, and a total  
519 sink of  $528 \pm 2$  Tg  $\text{a}^{-1}$ . The total emission is at the low end of the 538-593 Tg  $\text{a}^{-1}$  range reported for the  
520 2008-2017 decade by the Global Carbon Project (Saunio et al., 2020). Our joint inversion yields a  
521 methane lifetime against OH oxidation of  $11.2 \pm 0.1$  years, compared to the observationally-based estimate  
522 of  $11.2 \pm 1.3$  years (Prather et al., 2012), and pushes the northern to southern hemispheric OH ratio (0.98  
523 in GOSAT + in situ inversion versus 1.16 in prior estimate) closer to observed values ( $0.97 \pm 0.12$ ) (Patra  
524 et al., 2014).

525

#### 526 **4 Conclusions**

527 We quantify and attribute global sources, sinks, and trends of atmospheric methane for 2010-2017 by  
528 inversions of GOSAT satellite data and the GLOBALVIEWplus in situ methane observations from surface  
529 sites, towers, ships, and aircraft. The inversions use an analytical solution to Bayesian optimization  
530 problem including closed-form error covariance matrices from which the detailed information content of  
531 the inversion can be derived. We conduct inversions using GOSAT and in situ data separately and  
532 combined. In this manner we are able to quantify the consistency and complementarity (or redundancy)  
533 of the satellite and in situ observations.

534

535 We find that the GOSAT and in situ data are generally consistent and can fit each other independently  
536 through our inversions. Nevertheless, the GOSAT-only inversion has difficulty to fit the in situ  
537 observations in source regions (US and Europe), while In situ-only inversions could not reproduce the  
538 interannual variability of methane growth rate due to its heavy weighting to the northern mid-latitudes.  
539 The GOSAT + in situ inversion shows the best agreement with observations.

540

541 GOSAT and in situ observations are to a large extent complementary in terms of constraining global  
542 emissions. GOSAT provides stronger constraints than in situ observations for the tropics, while in situ  
543 observations are more important in US, Canada, Europe, and northern China where observations are dense.  
544 The joint GOSAT + in situ inversion reveals large underestimates of oil/gas emissions in the US and  
545 Canada, and large overestimates of coal emissions in China, relative to the national inventories reported  
546 to the United Nations Framework Convention on Climate Change (UNFCCC) and used here as prior  
547 estimates for our inversions. Emissions from boreal wetlands are overestimated in the mean WetCHARTs  
548 inventory used as prior estimate, particularly in May-June when snow cover and frozen soils inhibit  
549 methane emission.



550

551 Our inversions estimate increasing trends in US anthropogenic emissions driven by oil/gas production  
552 but decreasing trends in Canada (oil/gas) and Europe. Joint inversion of GOSAT and in situ data show  
553 weak decreasing trend in Chinese coal emissions for 2010-2017, consistent with a recent bottom-up  
554 inventory (Sheng et al., 2019).

555

556 We find that GOSAT and in situ observations are also complementary in constraining global methane  
557 budget. While the global budget information relies more on GOSAT observations, information from the  
558 in situ observations at northern mid-latitudes avoids the large error correlations between methane  
559 emissions and sink from OH and also corrects the underestimation of both emission and OH in the  
560 GOSAT-only inversion. Our joint GOSAT + in situ inversion yields the global methane emissions and  
561 loss of  $551 \pm 2$  and  $528 \pm 2$  Tg  $\text{a}^{-1}$  averaged over 2010-2017, and methane lifetime of  $11.2 \pm 0.1$  years.

562

563 Our study presents a framework to integrate satellite and in situ data in analytical inversions. We conclude  
564 that on the basis of the present observation system, in situ and satellite observations are complementary  
565 for constraining global methane budgets and regional emissions. Satellite observations of atmospheric  
566 methane are presently expanding with the new availability of global daily data from the TROPOMI  
567 instrument launched in October 2018 (Hu et al., 2018). In situ observations as presented in this paper will  
568 continue to play a critical role for satellite validation and for quantification of long-term trends. Their role  
569 for source characterization in supplement to satellite data will need to be re-evaluated as satellite  
570 observations expand, and the framework presented in this paper provides a means for doing so.

571

#### 572 **Data availability**

573 The GLOBALVIEWplus CH<sub>4</sub> ObsPack v1.0 data product is available at  
574 [https://www.esrl.noaa.gov/gmd/ccgg/obspace/data.php?id=obspace\\_ch4\\_1\\_GLOBALVIEWplus\\_v1.0\\_2019-01-08](https://www.esrl.noaa.gov/gmd/ccgg/obspace/data.php?id=obspace_ch4_1_GLOBALVIEWplus_v1.0_2019-01-08)  
575 (last access: July 17, 2020). The GOSAT proxy satellite methane observations are available  
576 at <https://doi.org/10.5285/18ef8247f52a4cb6a14013f8235cc1eb> (last access: July 17, 2020). Modeling  
577 data can be accessed by contacting the corresponding authors Xiao Lu (xiaolu@g.harvard.edu) and  
578 Yuzhong Zhang (zhangyuzhong@westlake.edu.cn).

579

#### 580 **Author contributions**

581 XL and DJJ designed the study. XL and YZZ conducted the modeling and data analyses with contributions  
582 from JDM, MPS, LS, ZQ, TRS, HON, RMY, and JXS. AA contributed to the GLOBALVIEWplus CH<sub>4</sub>  
583 ObsPack v1.0 data product. RJP and HB contributed to the GOSAT satellite methane retrievals. AAB and  
584 SM contributed to the WetCHARTs wetland emission inventory and its interpretation. XL and DJJ wrote  
585 the paper with input from all authors.

586

#### 587 **Competing interests**

588 The authors declare that they have no conflict of interest.



589

## 590 **Acknowledgement**

591 This work was supported by the NOAA AC4 program. RJP and HB are funded via the UK National Centre  
592 for Earth Observation (NCEO grant numbers: NE/R016518/1 and NE/N018079/1). RJP and HB  
593 acknowledge funding from the ESA GHG-CCI and Copernicus C3S projects. We thank the Japanese  
594 Aerospace Exploration Agency, National Institute for Environmental Studies, and the Ministry of  
595 Environment for the GOSAT data and their continuous support as part of the Joint Research Agreement.  
596 This research used the ALICE High Performance Computing Facility at the University of Leicester for  
597 the GOSAT retrievals. Part of this research was carried out at the Jet Propulsion Laboratory, California  
598 Institute of Technology, under a contract with the National Aeronautics and Space Administration.

599

600 We acknowledge all data providers/laboratories (<https://search.datacite.org/works/10.25925/20190108>)  
601 contributed to the GLOBALVIEWplus CH<sub>4</sub> ObsPack v1.0 data product compiled by NOAA Global  
602 Monitoring Laboratory. We acknowledge methane observations collected from the CONTRAIL  
603 (Comprehensive Observation Network for TRace gases by AirLiner) project (Machida et al., 2019). Data  
604 collected at WLEF Park Falls towers were supported by the NSF DEB-0845166 and DOE Ameriflux  
605 Network Management Project. Data collected at the Southern Great Plains were supported by the Office  
606 of Biological and Environmental Research of the US Department of Energy under contract no. DE-AC02-  
607 05CH11231 as part of the Atmospheric Radiation Measurement (ARM) Program, ARM Aerial Facility  
608 (AAF), and Terrestrial Ecosystem Science (TES) Program.

609

## 610 **Reference**

- 611 Alexe, M., Bergamaschi, P., Segers, A., Detmers, R., Butz, A., Hasekamp, O., Guerlet, S., Parker, R., Boesch, H., Frankenberg,  
612 C., Scheepmaker, R. A., Dlugokencky, E., Sweeney, C., Wofsy, S. C., and Kort, E. A.: Inverse modelling of CH<sub>4</sub> emissions  
613 for 2010–2011 using different satellite retrieval products from GOSAT and SCIAMACHY, *Atmos. Chem. Phys.*, 15, 113-  
614 133, <http://doi.org/10.5194/acp-15-113-2015>, 2015.
- 615 Alvarez, R. A., Zavala-Araiza, D., Lyon, D. R., Allen, D. T., Barkley, Z. R., Brandt, A. R., Davis, K. J., Herndon, S. C., Jacob,  
616 D. J., Karion, A., Kort, E. A., Lamb, B. K., Lauvaux, T., Maasakkers, J. D., Marchese, A. J., Omara, M., Pacala, S. W.,  
617 Peischl, J., Robinson, A. L., Shepson, P. B., Sweeney, C., Townsend-Small, A., Wofsy, S. C., and Hamburg, S. P.:  
618 Assessment of methane emissions from the U.S. oil and gas supply chain, *Science*, 361, 186-188,  
619 <http://doi.org/10.1126/science.aar7204>, 2018.
- 620 Bergamaschi, P., Frankenberg, C., Meirink, J. F., Krol, M., Dentener, F., Wagner, T., Platt, U., Kaplan, J. O., Körner, S.,  
621 Heimann, M., Dlugokencky, E. J., and Goede, A.: Satellite cartography of atmospheric methane from SCIAMACHY on  
622 board ENVISAT: 2. Evaluation based on inverse model simulations, *J. Geophys. Res.*, 112,  
623 <http://doi.org/10.1029/2006jd007268>, 2007.
- 624 Bergamaschi, P., Frankenberg, C., Meirink, J. F., Krol, M., Villani, M. G., Houweling, S., Dentener, F., Dlugokencky, E. J.,  
625 Miller, J. B., Gatti, L. V., Engel, A., and Levin, I.: Inverse modeling of global and regional CH<sub>4</sub> emissions using  
626 SCIAMACHY satellite retrievals, *J. Geophys. Res.*, 114, <http://doi.org/10.1029/2009jd012287>, 2009.
- 627 Bergamaschi, P., Houweling, S., Segers, A., Krol, M., Frankenberg, C., Scheepmaker, R. A., Dlugokencky, E., Wofsy, S. C.,  
628 Kort, E. A., Sweeney, C., Schuck, T., Brenninkmeijer, C., Chen, H., Beck, V., and Gerbig, C.: Atmospheric CH<sub>4</sub> in the  
629 first decade of the 21st century: Inverse modeling analysis using SCIAMACHY satellite retrievals and NOAA surface  
630 measurements, *J. Geophys. Res.*, 118, 7350-7369, <http://doi.org/10.1002/jgrd.50480>, 2013.



- 631 Bey, I., Jacob, D. J., Yantosca, R. M., Logan, J. A., Field, B. D., Fiore, A. M., Li, Q., Liu, H. Y., Mickley, L. J., and Schultz,  
632 M. G.: Global modeling of tropospheric chemistry with assimilated meteorology: Model description and evaluation, *J.*  
633 *Geophys. Res.*, 106, 23073-23095, <http://doi.org/10.1029/2001jd000807>, 2001.
- 634 Bloom, A. A., Bowman, K. W., Lee, M., Turner, A. J., Schroeder, R., Worden, J. R., Weidner, R., McDonald, K. C., and Jacob,  
635 D. J.: A global wetland methane emissions and uncertainty dataset for atmospheric chemical transport models  
636 (WetCHARTs version 1.0), *Geoscientific Model Development*, 10, 2141-2156, <http://doi.org/10.5194/gmd-10-2141-2017>,  
637 2017.
- 638 Bousquet, P., Ringeval, B., Pison, I., Dlugokencky, E. J., Brunke, E. G., Carouge, C., Chevallier, F., Fortems-Cheiney, A.,  
639 Frankenberg, C., Hauglustaine, D. A., Krummel, P. B., Langenfelds, R. L., Ramonet, M., Schmidt, M., Steele, L. P., Szopa,  
640 S., Yver, C., Viovy, N., and Ciais, P.: Source attribution of the changes in atmospheric methane for 2006–2008, *Atmos.*  
641 *Chem. Phys.*, 11, 3689-3700, <http://doi.org/10.5194/acp-11-3689-2011>, 2011.
- 642 Brasseur, G. P., and Jacob, D. J.: *Modeling of Atmospheric Chemistry*, Cambridge University Press,  
643 <http://doi.org/10.1017/9781316544754>, 2017.
- 644 Bruhwiler, L., Dlugokencky, E., Masarie, K., Ishizawa, M., Andrews, A., Miller, J., Sweeney, C., Tans, P., and Worthy, D.:  
645 CarbonTracker-CH4: an assimilation system for estimating emissions of atmospheric methane, *Atmos. Chem. Phys.*, 14,  
646 8269-8293, <http://doi.org/10.5194/acp-14-8269-2014>, 2014.
- 647 Bruhwiler, L. M., Basu, S., Bergamaschi, P., Bousquet, P., Dlugokencky, E., Houweling, S., Ishizawa, M., Kim, H. S., Locatelli,  
648 R., Maksyutov, S., Montzka, S., Pandey, S., Patra, P. K., Petron, G., Saunio, M., Sweeney, C., Schwietzke, S., Tans, P.,  
649 and Weatherhead, E. C.: U.S. CH4 emissions from oil and gas production: Have recent large increases been detected?, *J.*  
650 *Geophys. Res.*, 122, 4070-4083, <http://doi.org/10.1002/2016jd026157>, 2017.
- 651 Buchwitz, M., Reuter, M., Schneising, O., Boesch, H., Guerlet, S., Dils, B., Aben, I., Armante, R., Bergamaschi, P.,  
652 Blumenstock, T., Bovensmann, H., Brunner, D., Buchmann, B., Burrows, J. P., Butz, A., Chédin, A., Chevallier, F.,  
653 Crevoisier, C. D., Deutscher, N. M., Frankenberg, C., Hase, F., Hasekamp, O. P., Heymann, J., Kaminski, T., Laeng, A.,  
654 Lichtenberg, G., De Mazière, M., Noël, S., Notholt, J., Orphal, J., Popp, C., Parker, R., Scholze, M., Sussmann, R., Stiller,  
655 G. P., Warneke, T., Zehner, C., Bril, A., Crisp, D., Griffith, D. W. T., Kuze, A., O'Dell, C., Oshchepkov, S., Sherlock, V.,  
656 Suto, H., Wennberg, P., Wunch, D., Yokota, T., and Yoshida, Y.: The Greenhouse Gas Climate Change Initiative (GHG-  
657 CCI): Comparison and quality assessment of near-surface-sensitive satellite-derived CO2 and CH4 global data sets,  
658 *Remote Sens. Environ.*, 162, 344-362, <http://doi.org/10.1016/j.rse.2013.04.024>, 2015.
- 659 Butz, A., Guerlet, S., Hasekamp, O., Schepers, D., Galli, A., Aben, I., Frankenberg, C., Hartmann, J. M., Tran, H., Kuze, A.,  
660 Keppel-Aleks, G., Toon, G., Wunch, D., Wennberg, P., Deutscher, N., Griffith, D., Macatangay, R., Messerschmidt, J.,  
661 Notholt, J., and Warneke, T.: Toward accurate CO2 and CH4 observations from GOSAT, *Geophys. Res. Lett.*, 38, n/a-n/a,  
662 <http://doi.org/10.1029/2011gl047888>, 2011.
- 663 Calisesi, Y., Soebijanta, V. T., and van Oss, R.: Regridding of remote soundings: Formulation and application to ozone profile  
664 comparison, *J. Geophys. Res.*, 110, <http://doi.org/10.1029/2005jd006122>, 2005.
- 665 Cooperative Global Atmospheric Data Integration Project: Multi-laboratory compilation of atmospheric methane data for the  
666 period 1957-2017; `obspack_ch4_1_GLOBALVIEWplus_v1.0_2019_01_08`; NOAA Earth System Research Laboratory,  
667 Global Monitoring Laboratory. <http://dx.doi.org/10.25925/20190108>, 2019
- 668 Cressot, C., Chevallier, F., Bousquet, P., Crevoisier, C., Dlugokencky, E. J., Fortems-Cheiney, A., Frankenberg, C., Parker, R.,  
669 Pison, I., Scheepmaker, R. A., Montzka, S. A., Krummel, P. B., Steele, L. P., and Langenfelds, R. L.: On the consistency  
670 between global and regional methane emissions inferred from SCIAMACHY, TANSO-FTS, IASI and surface  
671 measurements, *Atmos. Chem. Phys.*, 14, 577-592, <http://doi.org/10.5194/acp-14-577-2014>, 2014.
- 672 Cui, Y. Y., Henze, D. K., Brioude, J., Angevine, W. M., Liu, Z., Bousserez, N., Guerrette, J., McKeen, S. A., Peischl, J., Yuan,  
673 B., Ryerson, T., Frost, G., and Trainer, M.: Inversion Estimates of Lognormally Distributed Methane Emission Rates  
674 From the Haynesville-Bossier Oil and Gas Production Region Using Airborne Measurements, *J. Geophys. Res.*, 124,  
675 3520-3531, <http://doi.org/10.1029/2018jd029489>, 2019.



- 676 Cusworth, D. H., Jacob, D. J., Sheng, J.-X., Benmergui, J., Turner, A. J., Brandman, J., White, L., and Randles, C. A.: Detecting  
677 high-emitting methane sources in oil/gas fields using satellite observations, *Atmos. Chem. Phys.*, 18, 16885-16896,  
678 <http://doi.org/10.5194/acp-18-16885-2018>, 2018.
- 679 Dlugokencky, E. J., Bruhwiler, L., White, J. W. C., Emmons, L. K., Novelli, P. C., Montzka, S. A., Masarie, K. A., Lang, P. M.,  
680 Croftwell, A. M., Miller, J. B., and Gatti, L. V.: Observational constraints on recent increases in the atmospheric  
681 CH<sub>4</sub> burden, *Geophys. Res. Lett.*, 36, <http://doi.org/10.1029/2009gl039780>, 2009.
- 682 Etiope, G., Ciotoli, G., Schwietzke, S., and Schoell, M.: Gridded maps of geological methane emissions and their isotopic  
683 signature, *Earth System Science Data*, 11, 1-22, <http://doi.org/10.5194/essd-11-1-2019>, 2019.
- 684 Franco, B., Mahieu, E., Emmons, L. K., Tzompa-Sosa, Z. A., Fischer, E. V., Sudo, K., Bovy, B., Conway, S., Griffin, D.,  
685 Hannigan, J. W., Strong, K., and Walker, K. A.: Evaluating ethane and methane emissions associated with the development  
686 of oil and natural gas extraction in North America, *Environmental Research Letters*, 11, 044010,  
687 <http://doi.org/10.1088/1748-9326/11/4/044010>, 2016.
- 688 Fraser, A., Palmer, P. I., Feng, L., Boesch, H., Cogan, A., Parker, R., Dlugokencky, E. J., Fraser, P. J., Krummel, P. B.,  
689 Langenfelds, R. L., and Doherty, S., Prinn, R. G., Steele, L. P., van der Schoot, M., and Weiss, R. F.: Estimating  
690 regional methane surface fluxes: the relative importance of surface and GOSAT mole fraction measurements, *Atmos.*  
691 *Chem. Phys.*, 13, 5697-5713, <http://doi.org/10.5194/acp-13-5697-2013>, 2013.
- 692 Fung, I., John, J., Lerner, J., Matthews, E., Prather, M., Steele, L. P., and Fraser, P. J.: Three-dimensional model synthesis of  
693 the global methane cycle, *J. Geophys. Res.*, 96, 13033, <http://doi.org/10.1029/91jd01247>, 1991.
- 694 Ganesan, A. L., Rigby, M., Lunt, M. F., Parker, R. J., Boesch, H., Goulding, N., Umezawa, T., Zahn, A., Chatterjee, A., Prinn,  
695 R. G., Tiwari, Y. K., van der Schoot, M., and Krummel, P. B.: Atmospheric observations show accurate reporting and little  
696 growth in India's methane emissions, *Nat Commun*, 8, 836, <http://doi.org/10.1038/s41467-017-00994-7>, 2017.
- 697 Gelaro, R., McCarty, W., Suárez, M. J., Todling, R., Molod, A., Takacs, L., Randles, C. A., Darmenov, A., Bosilovich, M. G.,  
698 Reichle, R., Wargan, K., Coy, L., Cullather, R., Draper, C., Akella, S., Buchard, V., Conaty, A., da Silva, A. M., Gu, W.,  
699 Kim, G.-K., Koster, R., Lucchesi, R., Merkova, D., Nielsen, J. E., Partyka, G., Pawson, S., Putman, W., Rienecker, M.,  
700 Schubert, S. D., Sienkiewicz, M., and Zhao, B.: The Modern-Era Retrospective Analysis for Research and Applications,  
701 Version 2 (MERRA-2), *J. Clim.*, 30, 5419-5454, <http://doi.org/10.1175/jcli-d-16-0758.1>, 2017.
- 702 Hausmann, P., Sussmann, R., and Smale, D.: Contribution of oil and natural gas production to renewed increase in atmospheric  
703 methane (2007–2014): top-down estimate from ethane and methane column observations, *Atmos. Chem. Phys.*, 16, 3227-  
704 3244, <http://doi.org/10.5194/acp-16-3227-2016>, 2016.
- 705 Heald, C. L., Jacob, D. J., Jones, D. B. A., Palmer, P. I., Logan, J. A., Streets, D. G., Sachse, G. W., Gille, J. C., Hoffman, R.  
706 N., and Nehrkor, T.: Comparative inverse analysis of satellite (MOPITT) and aircraft (TRACE-P) observations to  
707 estimate Asian sources of carbon monoxide, *J. Geophys. Res.*, 109, <http://doi.org/10.1029/2004jd005185>, 2004.
- 708 Helmig, D., Rossabi, S., Hueber, J., Tans, P., Montzka, S. A., Masarie, K., Thoning, K., Plass-Duelmer, C., Claude, A.,  
709 Carpenter, L. J., Lewis, A. C., Punjabi, S., Reimann, S., Vollmer, M. K., Steinbrecher, R., Hannigan, J. W., Emmons, L.  
710 K., Mahieu, E., Franco, B., Smale, D., and Pozzer, A.: Reversal of global atmospheric ethane and propane trends largely  
711 due to US oil and natural gas production, *Nature Geosci.*, 9, 490-495, <http://doi.org/10.1038/ngeo2721>, 2016.
- 712 Hmiel, B., Petrenko, V. V., Dyonisius, M. N., Buizert, C., Smith, A. M., Place, P. F., Harth, C., Beaudette, R., Hua, Q., Yang,  
713 B., Vimont, I., Michel, S. E., Severinghaus, J. P., Etheridge, D., Bromley, T., Schmitt, J., Faïn, X., Weiss, R. F., and  
714 Dlugokencky, E.: Preindustrial 14CH<sub>4</sub> indicates greater anthropogenic fossil CH<sub>4</sub> emissions, *Nature*, 578, 409-412,  
715 <http://doi.org/10.1038/s41586-020-1991-8>, 2020.
- 716 Holmes, C. D., Prather, M. J., Søvde, O. A., and Myhre, G.: Future methane, hydroxyl, and their uncertainties: key climate and  
717 emission parameters for future predictions, *Atmos. Chem. Phys.*, 13, 285-302, <http://doi.org/10.5194/acp-13-285-2013>,  
718 2013.
- 719 Houweling, S., Krol, M., Bergamaschi, P., Frankenberg, C., Dlugokencky, E. J., Morino, I., Notholt, J., Sherlock, V., Wunch,  
720 D., Beck, V., Gerbig, C., Chen, H., Kort, E. A., Röckmann, T., and Aben, I.: A multi-year methane inversion using



- 721 SCIAMACHY, accounting for systematic errors using TCCON measurements, *Atmos. Chem. Phys.*, 14, 3991-4012,  
722 <http://doi.org/10.5194/acp-14-3991-2014>, 2014.
- 723 Houweling, S., Bergamaschi, P., Chevallier, F., Heimann, M., Kaminski, T., Krol, M., Michalak, A. M., and Patra, P.: Global  
724 inverse modeling of CH<sub>4</sub> sources and sinks: an overview of methods, *Atmos. Chem. Phys.*, 17, 235-256,  
725 <http://doi.org/10.5194/acp-17-235-2017>, 2017.
- 726 Hu, H., Landgraf, J., Detmers, R., Borsdorff, T., Aan de Brugh, J., Aben, I., Butz, A., and Hasekamp, O.: Toward Global  
727 Mapping of Methane With TROPOMI: First Results and Intersatellite Comparison to GOSAT, *Geophys. Res. Lett.*, 45,  
728 3682-3689, <http://doi.org/10.1002/2018gl077259>, 2018.
- 729 Jacob, D. J., Turner, A. J., Maasakkers, J. D., Sheng, J., Sun, K., Liu, X., Chance, K., Aben, I., McKeever, J., and Frankenberg,  
730 C.: Satellite observations of atmospheric methane and their value for quantifying methane emissions, *Atmos. Chem. Phys.*,  
731 16, 14371-14396, <http://doi.org/10.5194/acp-16-14371-2016>, 2016.
- 732 Janardanan, R., Maksyutov, S., Tsuruta, A., Wang, F., Tiwari, Y. K., Valsala, V., Ito, A., Yoshida, Y., Kaiser, J. W., Janssens-  
733 Maenhout, G., Arshinov, M., Sasakawa, M., Tohjima, Y., Worthy, D. E. J., Dlugokencky, E. J., Ramonet, M., Arduini, J.,  
734 Lavric, J. V., Piacentino, S., Krummel, P. B., Langenfelds, R. L., Mammarella, I., and Matsunaga, T.: Country-Scale  
735 Analysis of Methane Emissions with a High-Resolution Inverse Model Using GOSAT and Surface Observations, *Remote*  
736 *Sensing*, 12, 375, <http://doi.org/10.3390/rs12030375>, 2020.
- 737 Janssens-Maenhout, G., Crippa, M., Guizzardi, D., Muntean, M., Schaaf, E., Dentener, F., Bergamaschi, P., Pagliari, V., Olivier,  
738 J. G. J., Peters, J. A. H. W., van Aardenne, J. A., Monni, S., Doering, U., Petrescu, A. M. R., Solazzo, E., and Oreggioni,  
739 G. D.: EDGAR v4.3.2 Global Atlas of the three major greenhouse gas emissions for the period 1970–2012, *Earth System*  
740 *Science Data*, 11, 959-1002, <http://doi.org/10.5194/essd-11-959-2019>, 2019.
- 741 Koo, J.-H., Walker, K. A., Jones, A., Sheese, P. E., Boone, C. D., Bernath, P. F., and Manney, G. L.: Global climatology based  
742 on the ACE-FTS version 3.5 dataset: Addition of mesospheric levels and carbon-containing species in the UTLS, *J. Quant.*  
743 *Spectrosc. Radiat. Transfer*, 186, 52-62, <http://doi.org/10.1016/j.jqsrt.2016.07.003>, 2017.
- 744 Kuze, A., Suto, H., Shiomi, K., Kawakami, S., Tanaka, M., Ueda, Y., Deguchi, A., Yoshida, J., Yamamoto, Y., Kataoka, F.,  
745 Taylor, T. E., and Buijs, H. L.: Update on GOSAT TANSO-FTS performance, operations, and data products after more  
746 than 6 years in space, *Atmospheric Measurement Techniques*, 9, 2445-2461, <http://doi.org/10.5194/amt-9-2445-2016>,  
747 2016.
- 748 Lan, X., Tans, P., Sweeney, C., Andrews, A., Dlugokencky, E., Schwietzke, S., Kofler, J., McKain, K., Thoning, K., Crotwell,  
749 M., Montzka, S., Miller, B. R., and Biraud, S. C.: Long-Term Measurements Show Little Evidence for Large Increases in  
750 Total U.S. Methane Emissions Over the Past Decade, *Geophys. Res. Lett.*, 46, 4991-4999,  
751 <http://doi.org/10.1029/2018gl081731>, 2019.
- 752 Lunt, M. F., Palmer, P. I., Feng, L., Taylor, C. M., Boesch, H., and Parker, R. J.: An increase in methane emissions from tropical  
753 Africa between 2010 and 2016 inferred from satellite data, *Atmos. Chem. Phys.*, 19, 14721-14740,  
754 <http://doi.org/10.5194/acp-19-14721-2019>, 2019.
- 755 Maasakkers, J. D., Jacob, D. J., Sulprizio, M. P., Turner, A. J., Weitz, M., Wirth, T., Hight, C., DeFigueiredo, M., Desai, M.,  
756 Schmeltz, R., Hockstad, L., Bloom, A. A., Bowman, K. W., Jeong, S., and Fischer, M. L.: Gridded National Inventory of  
757 U.S. Methane Emissions, *Environ. Sci. Technol.*, 50, 13123-13133, <http://doi.org/10.1021/acs.est.6b02878>, 2016.
- 758 Maasakkers, J. D., Jacob, D. J., Sulprizio, M. P., Scarpelli, T. R., Nesser, H., Sheng, J.-X., Zhang, Y., Hersher, M., Bloom, A.  
759 A., Bowman, K. W., Worden, J. R., Janssens-Maenhout, G., and Parker, R. J.: Global distribution of methane emissions,  
760 emission trends, and OH concentrations and trends inferred from an inversion of GOSAT satellite data for 2010–2015,  
761 *Atmos. Chem. Phys.*, 19, 7859-7881, <http://doi.org/10.5194/acp-19-7859-2019>, 2019.
- 762 Maasakkers J. D., Jacob, D. J., Sulprizio, M. P., Scarpelli, T. R., Nesser, H., Sheng, J.-X., Zhang, Y., Lu, X., Bloom, A. A.,  
763 Bowman, K. W., Worden, J. R., and Parker, R. J.: 2010-2015 North American methane emissions, sectoral contributions,  
764 and trends: a high-resolution inversion of GOSAT satellite observations of atmospheric methane, submitted to *Atmos.*  
765 *Chem. Phys.*, file available at <http://acmg.seas.harvard.edu/publications/2020/maasakkers2020.pdf>.



- 766 Machida T., H. Matsueda, Y. Sawa and Y. Niwa, Atmospheric trace gas data from the CONTRAIL flask air sampling over the  
767 Pacific Ocean, Center for Global Environmental Research, NIES, DOI:10.17595/20190828.001., 2019
- 768 McNorton, J., Wilson, C., Gloor, M., Parker, R. J., Boesch, H., Feng, W., Hossaini, R., and Chipperfield, M. P.: Attribution of  
769 recent increases in atmospheric methane through 3-D inverse modelling, *Atmos. Chem. Phys.*, 18, 18149-18168,  
770 <http://doi.org/10.5194/acp-18-18149-2018>, 2018.
- 771 Miller, S. M., Wofsy, S. C., Michalak, A. M., Kort, E. A., Andrews, A. E., Biraud, S. C., Dlugokencky, E. J., Eluszkiewicz, J.,  
772 Fischer, M. L., Janssens-Maenhout, G., Miller, B. R., Miller, J. B., Montzka, S. A., Nehrkorn, T., and Sweeney, C.:  
773 Anthropogenic emissions of methane in the United States, *Proc. Natl. Acad. Sci. U. S. A.*, 110, 20018-20022,  
774 <http://doi.org/10.1073/pnas.1314392110>, 2013.
- 775 Miller, S. M., Michalak, A. M., Detmers, R. G., Hasekamp, O. P., Bruhwiler, L. M. P., and Schwietzke, S.: China's coal mine  
776 methane regulations have not curbed growing emissions, *Nat Commun*, 10, 303, [http://doi.org/10.1038/s41467-018-](http://doi.org/10.1038/s41467-018-07891-7)  
777 [07891-7](http://doi.org/10.1038/s41467-018-07891-7), 2019.
- 778 Monteil, G., Houweling, S., Butz, A., Guerlet, S., Schepers, D., Hasekamp, O., Frankenberg, C., Scheepmaker, R., Aben, I.,  
779 and Röckmann, T.: Comparison of CH<sub>4</sub> inversions based on 15 months of GOSAT and SCIAMACHY observations, *J.*  
780 *Geophys. Res.*, 118, 11,807-811,823, <http://doi.org/10.1002/2013jd019760>, 2013.
- 781 Murguía-Flores, F., Arndt, S., Ganesan, A. L., Murray-Tortarolo, G., and Hornibrook, E. R. C.: Soil Methanotrophy Model  
782 (MeMo v1.0): a process-based model to quantify global uptake of atmospheric methane by soil, *Geoscientific Model*  
783 *Development*, 11, 2009-2032, <http://doi.org/10.5194/gmd-11-2009-2018>, 2018.
- 784 Murray, L. T., Jacob, D. J., Logan, J. A., Hudman, R. C., and Koshak, W. J.: Optimized regional and interannual variability of  
785 lightning in a global chemical transport model constrained by LIS/OTD satellite data, *J. Geophys. Res.*, 117, D20307,  
786 <http://doi.org/10.1029/2012jd017934>, 2012.
- 787 Naik, V., Voulgarakis, A., Fiore, A. M., Horowitz, L. W., Lamarque, J. F., Lin, M., Prather, M. J., Young, P. J., Bergmann, D.,  
788 Cameron-Smith, P. J., Cionni, I., Collins, W. J., Dalsøren, S. B., Doherty, R., Eyring, V., Faluvegi, G., Folberth, G. A.,  
789 Josse, B., Lee, Y. H., MacKenzie, I. A., Nagashima, T., van Noije, T. P. C., Plummer, D. A., Righi, M., Rumbold, S. T.,  
790 Skeie, R., Shindell, D. T., Stevenson, D. S., Strode, S., Sudo, K., Szopa, S., and Zeng, G.: Preindustrial to present-day  
791 changes in tropospheric hydroxyl radical and methane lifetime from the Atmospheric Chemistry and Climate Model  
792 Intercomparison Project (ACCMIP), *Atmos. Chem. Phys.*, 13, 5277-5298, <http://doi.org/10.5194/acp-13-5277-2013>,  
793 2013.
- 794 Parker, R. J., Webb, A., Boesch, H., Somkuti, P., Barrio Guillo, R., Di Noia, A., Kalaitzi, N., Anand, J., Bergamaschi, P.,  
795 Chevallier, F., Palmer, P. I., Feng, L., Deutscher, N. M., Feist, D. G., Griffith, D. W. T., Hase, F., Kivi, R., Morino, I.,  
796 Notholt, J., Oh, Y.-S., Ohyama, H., Petri, C., Pollard, D. F., Roehl, C., Sha, M. K., Shiomi, K., Strong, K., Sussmann, R.,  
797 Te, Y., Velasco, V. A., Warneke, T., Wennberg, P. O., and Wunch, D.: A Decade of GOSAT Proxy Satellite  
798 CH<sub>4</sub> Observations, *Earth Syst. Sci. Data Discuss.*, <https://doi.org/10.5194/essd-2020-114>, in review, 2020.
- 799 Patra, P. K., Houweling, S., Krol, M., Bousquet, P., Belikov, D., Bergmann, D., Bian, H., Cameron-Smith, P., Chipperfield, M.  
800 P., Corbin, K., Fortems-Cheiney, A., Fraser, A., Gloor, E., Hess, P., Ito, A., Kawa, S. R., Law, R. M., Loh, Z., Maksyutov,  
801 S., Meng, L., Palmer, P. I., Prinn, R. G., Rigby, M., Saito, R., and Wilson, C.: TransCom model simulations of CH<sub>4</sub> and  
802 related species: linking transport, surface flux and chemical loss with CH<sub>4</sub> variability in the troposphere and lower  
803 stratosphere, *Atmos. Chem. Phys.*, 11, 12813-12837, <http://doi.org/10.5194/acp-11-12813-2011>, 2011.
- 804 Patra, P. K., Krol, M. C., Montzka, S. A., Arnold, T., Atlas, E. L., Lintner, B. R., Stephens, B. B., Xiang, B., Elkins, J. W.,  
805 Fraser, P. J., Ghosh, A., Hints, E. J., Hurst, D. F., Ishijima, K., Krümmel, P. B., Miller, B. R., Miyazaki, K., Moore, F. L.,  
806 Muhle, J., O'Doherty, S., Prinn, R. G., Steele, L. P., Takigawa, M., Wang, H. J., Weiss, R. F., Wofsy, S. C., and Young, D.:  
807 Observational evidence for interhemispheric hydroxyl-radical parity, *Nature*, 513, 219-223,  
808 <http://doi.org/10.1038/nature13721>, 2014.
- 809 Patra, P. K., Saeki, T., Dlugokencky, E. J., Ishijima, K., Umezawa, T., Ito, A., Aoki, S., Morimoto, S., Kort, E. A., Crotwell,  
810 A., Ravi Kumar, K., and Nakazawa, T.: Regional Methane Emission Estimation Based on Observed Atmospheric



- 811 Concentrations (2002-2012), *Journal of the Meteorological Society of Japan*. Ser. II, 94, 91-113,  
812 <http://doi.org/10.2151/jmsj.2016-006>, 2016.
- 813 Pickett-Heaps, C. A., Jacob, D. J., Wecht, K. J., Kort, E. A., Wofsy, S. C., Diskin, G. S., Worthy, D. E. J., Kaplan, J. O., Bey,  
814 I., and Drevet, J.: Magnitude and seasonality of wetland methane emissions from the Hudson Bay Lowlands (Canada),  
815 *Atmos. Chem. Phys.*, 11, 3773-3779, <http://doi.org/10.5194/acp-11-3773-2011>, 2011.
- 816 Pison, I., Bousquet, P., Chevallier, F., Szopa, S., and Hauglustaine, D.: Multi-species inversion of CH<sub>4</sub>, CO and H<sub>2</sub> emissions  
817 from surface measurements, *Atmos. Chem. Phys.*, 9, 5281-5297, <http://doi.org/10.5194/acp-9-5281-2009>, 2009.
- 818 Prather, M. J., Holmes, C. D., and Hsu, J.: Reactive greenhouse gas scenarios: Systematic exploration of uncertainties and the  
819 role of atmospheric chemistry, *Geophys. Res. Lett.*, 39, n/a-n/a, <http://doi.org/10.1029/2012gl051440>, 2012.
- 820 Rodgers, C. D.: *Inverse Methods for Atmospheric Sounding: Theory and Practice*, 2000.
- 821 Saunois, M., Stavert, A. R., Poulter, B., Bousquet, P., Canadell, J. G., Jackson, R. B., Raymond, P. A., Dlugokencky, E. J.,  
822 Houweling, S., Patra, P. K., Ciais, P., Arora, V. K., Bastviken, D., Bergamaschi, P., Blake, D. R., Brailsford, G., Bruhwiler,  
823 L., Carlson, K. M., Carrol, M., Castaldi, S., Chandra, N., Crevoisier, C., Crill, P. M., Covey, K., Curry, C. L., Etiope, G.,  
824 Frankenberg, C., Gedney, N., Hegglin, M. I., Höglund-Isaksson, L., Hugelius, G., Ishizawa, M., Ito, A., Janssens-  
825 Maenhout, G., Jensen, K. M., Joos, F., Kleinen, T., Krummel, P. B., Langenfelds, R. L., Laruelle, G. G., Liu, L., Machida,  
826 T., Maksyutov, S., McDonald, K. C., McNorton, J., Miller, P. A., Melton, J. R., Morino, I., Müller, J., Murguía-Flores, F.,  
827 Naik, V., Niwa, Y., Noce, S., O'Doherty, S., Parker, R. J., Peng, C., Peng, S., Peters, G. P., Prigent, C., Prinn, R., Ramonet,  
828 M., Regnier, P., Riley, W. J., Rosentretter, J. A., Segers, A., Simpson, I. J., Shi, H., Smith, S. J., Steele, L. P., Thornton, B.  
829 F., Tian, H., Tohjima, Y., Tubiello, F. N., Tsuruta, A., Viovy, N., Voulgarakis, A., Weber, T. S., van Weele, M., van der  
830 Werf, G. R., Weiss, R. F., Worthy, D., Wunch, D., Yin, Y., Yoshida, Y., Zhang, W., Zhang, Z., Zhao, Y., Zheng, B., Zhu,  
831 Q., Zhu, Q., and Zhuang, Q.: The Global Methane Budget 2000–2017, *Earth System Science Data*, 12, 1561-1623,  
832 <http://doi.org/10.5194/essd-12-1561-2020>, 2020.
- 833 Scarpelli, T. R., Jacob, D. J., Maasackers, J. D., Sulprizio, M. P., Sheng, J.-X., Rose, K., Romeo, L., Worden, J. R., and  
834 Janssens-Maenhout, G.: A global gridded (0.1° x 0.1°) inventory of methane emissions from oil, gas, and coal  
835 exploitation based on national reports to the United Nations Framework Convention on Climate Change, *Earth System*  
836 *Science Data*, 12, 563-575, <http://doi.org/10.5194/essd-12-563-2020>, 2020.
- 837 Sheng, J.-X., Jacob, D. J., Turner, A. J., Maasackers, J. D., Sulprizio, M. P., Bloom, A. A., Andrews, A. E., and Wunch, D.:  
838 High-resolution inversion of methane emissions in the Southeast US using SEAC&lt;sup>4</sup>&lt;sup>RS</sup> aircraft  
839 observations of atmospheric methane: anthropogenic and wetland sources, *Atmos. Chem. Phys.*, 18, 6483-6491,  
840 <http://doi.org/10.5194/acp-18-6483-2018>, 2018.
- 841 Sheng, J., Song, S., Zhang, Y., Prinn, R. G., and Janssens-Maenhout, G.: Bottom-Up Estimates of Coal Mine Methane  
842 Emissions in China: A Gridded Inventory, Emission Factors, and Trends, *Environmental Science & Technology Letters*,  
843 6, 473-478, <http://doi.org/10.1021/acs.estlett.9b00294>, 2019.
- 844 Thompson, R. L., Stohl, A., Zhou, L. X., Dlugokencky, E., Fukuyama, Y., Tohjima, Y., Kim, S. Y., Lee, H., Nisbet, E. G.,  
845 Fisher, R. E., Lowry, D., Weiss, R. F., Prinn, R. G., O'Doherty, S., Young, D., and White, J. W. C.: Methane emissions in  
846 East Asia for 2000-2011 estimated using an atmospheric Bayesian inversion, *J. Geophys. Res.*, 120, 4352-4369,  
847 <http://doi.org/10.1002/2014jd022394>, 2015.
- 848 Turner, A. J., Jacob, D. J., Wecht, K. J., Maasackers, J. D., Lundgren, E., Andrews, A. E., Biraud, S. C., Boesch, H., Bowman,  
849 K. W., Deutscher, N. M., Dubey, M. K., Griffith, D. W. T., Hase, F., Kuze, A., Notholt, J., Ohyama, H., Parker, R., Payne,  
850 V. H., Sussmann, R., Sweeney, C., Velazco, V. A., Warneke, T., Wennberg, P. O., and Wunch, D.: Estimating global and  
851 North American methane emissions with high spatial resolution using GOSAT satellite data, *Atmos. Chem. Phys.*, 15,  
852 7049-7069, <http://doi.org/10.5194/acp-15-7049-2015>, 2015.
- 853 van der Werf, G. R., Randerson, J. T., Giglio, L., van Leeuwen, T. T., Chen, Y., Rogers, B. M., Mu, M., van Marle, M. J. E.,  
854 Morton, D. C., Collatz, G. J., Yokelson, R. J., and Kasibhatla, P. S.: Global fire emissions estimates during 1997–2016,  
855 *Earth System Science Data*, 9, 697-720, <http://doi.org/10.5194/essd-9-697-2017>, 2017.



- 856 Wang, X., Jacob, D. J., Eastham, S. D., Sulprizio, M. P., Zhu, L., Chen, Q., Alexander, B., Sherwen, T., Evans, M. J., Lee, B.  
857 H., Haskins, J. D., Lopez-Hilfiker, F. D., Thornton, J. A., Huey, G. L., and Liao, H.: The role of chlorine in global  
858 tropospheric chemistry, *Atmos. Chem. Phys.*, 19, 3981-4003, <http://doi.org/10.5194/acp-19-3981-2019>, 2019.
- 859 Waymark, C., Walker, K., Boone, C. D., and Bernath, P. F.: ACE-FTS version 3.0 data set: validation and data processing  
860 update., *ANNALS OF GEOPHYSICS*, 56, <http://doi.org/10.4401/ag-6339>, 2013.
- 861 Wecht, K. J., Jacob, D. J., Frankenberg, C., Jiang, Z., and Blake, D. R.: Mapping of North American methane emissions with  
862 high spatial resolution by inversion of SCIAMACHY satellite data, *J. Geophys. Res.*, 119, 7741-7756,  
863 <http://doi.org/10.1002/2014jd021551>, 2014.
- 864 Zhang, B., Tian, H., Ren, W., Tao, B., Lu, C., Yang, J., Banger, K., and Pan, S.: Methane emissions from global rice fields:  
865 Magnitude, spatiotemporal patterns, and environmental controls, *Global Biogeochem. Cycles*, 30, 1246-1263,  
866 <http://doi.org/10.1002/2016gb005381>, 2016.
- 867 Zhang, Y., Jacob, D. J., Maasakkers, J. D., Sulprizio, M. P., Sheng, J.-X., Gautam, R., and Worden, J.: Monitoring global  
868 tropospheric OH concentrations using satellite observations of atmospheric methane, *Atmos. Chem. Phys.*, 18, 15959-  
869 15973, <http://doi.org/10.5194/acp-18-15959-2018>, 2018.
- 870 Zhang, Y., Jacob, D., Scarpelli, T., Maasakkers, J. D., Sulprizio, M., Penn, E., Sheng, J. X., Bloom, A. A., and Worden, J.:  
871 Attribution of the 2010-2017 trend in atmospheric methane by improved inverse analysis of GOSAT satellite observations,  
872 AGU Fall meeting, 2019 (submitted to *Atmos. Chem. Phys.*, file available at  
873 [http://acmg.seas.harvard.edu/publications/2020/zhang\\_yuzhong2020ACP.pdf](http://acmg.seas.harvard.edu/publications/2020/zhang_yuzhong2020ACP.pdf))
- 874 Zhang, Y., Gautam, R., Pandey, S., Omara, M., Maasakkers, J. D., Sadavarte, P., Lyon, D., Nesser, H., Sulprizio, M. P., Varon,  
875 D. J., Zhang, R., Houweling, S., Zavala-Araiza, D., Alvarez, R. A., Lorente, A., Hamburg, S. P., Aben, I., and Jacob, D.  
876 J.: Quantifying methane emissions from the largest oil-producing basin in the United States from space, *Science Advances*,  
877 6, eaaz5120, <http://doi.org/10.1126/sciadv.aaz5120>, 2020.
- 878 Zhao, Y., Saunio, M., Bousquet, P., Lin, X., Berchet, A., Hegglin, M. I., Canadell, J. G., Jackson, R. B., Hauglustaine, D. A.,  
879 Szopa, S., Stavert, A. R., Abraham, N. L., Archibald, A. T., Bekki, S., Deushi, M., Jöckel, P., Josse, B., Kinnison, D.,  
880 Kirner, O., Marécal, V., Connor, F. M., Plummer, D. A., Revell, L. E., Rozanov, E., Stenke, A., Strode, S.,  
881 Tilmes, S., Dlugokencky, E. J., and Zheng, B.: Inter-model comparison of global hydroxyl radical (OH) distributions and  
882 their impact on atmospheric methane over the 2000&#2013;2016 period, *Atmos. Chem. Phys.*, 19, 13701-13723,  
883 <http://doi.org/10.5194/acp-19-13701-2019>, 2019.
- 884 Zona, D., Gioli, B., Commane, R., Lindaas, J., Wofsy, S. C., Miller, C. E., Dinardo, S. J., Dengel, S., Sweeney, C., Karion, A.,  
885 Chang, R. Y., Henderson, J. M., Murphy, P. C., Goodrich, J. P., Moreaux, V., Liljedahl, A., Watts, J. D., Kimball, J. S.,  
886 Lipson, D. A., and Oechel, W. C.: Cold season emissions dominate the Arctic tundra methane budget, *Proc. Natl. Acad.  
887 Sci. U. S. A.*, 113, 40-45, <http://doi.org/10.1073/pnas.1516017113>, 2016.
- 888



889 **Table 1.** Global sources and sinks of atmospheric methane, 2010-2017<sup>a</sup>.

|  | Prior <sup>b</sup> | Posterior <sup>c</sup> |
|--|--------------------|------------------------|
| <b>Total sources [Tg a<sup>-1</sup>]</b> | 533                | 551                    |
| <b>Natural Sources</b>                   |                    |                        |
| Wetlands                                 | 161                | 148                    |
| Open fires                               | 14                 | 16                     |
| Termites                                 | 12                 | 14                     |
| Seeps                                    | 2                  | 2                      |
| <b>Anthropogenic sources</b>             |                    |                        |
| Livestock                                | 117                | 136                    |
| Oil                                      | 42                 | 40                     |
| Natural gas                              | 25                 | 30                     |
| Coal mining                              | 31                 | 23                     |
| Rice cultivation                         | 38                 | 44                     |
| Wastewater                               | 37                 | 42                     |
| Landfills                                | 30                 | 31                     |
| Other Anthropogenic                      | 25                 | 25                     |
| <b>Total Sinks [Tg a<sup>-1</sup>]</b>   | 540                | 528                    |
| Tropospheric OH                          | 468                | 455                    |
| Stratospheric loss <sup>d</sup>          | 33                 | 33                     |
| Soil uptake <sup>d</sup>                 | 34                 | 34                     |
| Tropospheric Cl <sup>d</sup>             | 5                  | 5                      |

890 <sup>a</sup> 8-year mean values for 2010-2017.

891 <sup>b</sup> Prior natural source estimates (2000-2017 means) are from Bloom et al. (2017) for wetlands, Etiope et al. (2019) and  
892 Hmiel et al. (2020) for seeps, Fung et al. (1991) for termite emissions, van der Werf et al. (2017) for open fire emissions.  
893 Prior anthropogenic source estimates for 2012 are from EDGAR v4.3.2 (Janssens-Maenhout et al., 2017) except from  
894 Scarpelli et al. (2020) for fuel exploitation (oil, gas, coal), and are overwritten for the US with the gridded EPA inventory  
895 of Maasackers et al. (2016). The prior tropospheric OH concentration field is from Wecht et al. (2014) and yields a  
896 methane lifetime against oxidation by tropospheric OH of 10.6 years.

897 <sup>c</sup> From the joint inversion of GOSAT and in situ data

898 <sup>d</sup> These minor sinks are not optimized by the inversion.

899



900 **Table 2.** Anthropogenic methane emissions and trends, 2010-2017 <sup>a</sup>

| Inversions  | In situ-only<br>inversion | GOSAT-only<br>inversion | GOSAT+in situ<br>inversion |
|---|---------------------------|-------------------------|----------------------------|
| US <sup>b</sup> (prior: 28 Tg a <sup>-1</sup> )       |                           |                         |                            |
| Posterior (Tg a <sup>-1</sup> )                       | 35                        | 31                      | 36                         |
| 2010-2017 trend (Tg a <sup>-1</sup> a <sup>-1</sup> ) | 0.5                       | -0.1                    | 0.4                        |
| Canada (prior: 5 Tg a <sup>-1</sup> )                 |                           |                         |                            |
| Posterior (Tg a <sup>-1</sup> )                       | 8                         | 5                       | 8                          |
| 2010-2017 trend (Tg a <sup>-1</sup> a <sup>-1</sup> ) | -0.2                      | -0.0                    | -0.2                       |
| Europe <sup>c</sup> (prior: 27 Tg a <sup>-1</sup> )   |                           |                         |                            |
| Posterior (Tg a <sup>-1</sup> )                       | 28                        | 17                      | 23                         |
| 2010-2017 trend (Tg a <sup>-1</sup> a <sup>-1</sup> ) | 0.1                       | -0.6                    | -0.4                       |
| China (prior: 63 Tg a <sup>-1</sup> )                 |                           |                         |                            |
| Posterior (Tg a <sup>-1</sup> )                       | 45                        | 46                      | 43                         |
| 2010-2017 trend (Tg a <sup>-1</sup> a <sup>-1</sup> ) | 0.3                       | 0.4                     | 0.1                        |

901 <sup>a</sup> Posterior estimates of mean 2010-2017 emissions and trends for the In situ-only, GOSAT-only, and GOSAT + in situ  
902 joint inversions.

903 <sup>b</sup> Including contiguous US and Alaska.

904 <sup>c</sup> Europe is defined as west of 30°E, excluding Russia.

905

906

907



908 **Table 3.** Optimized global methane budget, 2010-2017.

909

| Inversions                                | In situ            | GOSAT              | GOSAT+in situ      |
|---|--------------------|--------------------|--------------------|
| <b>Total sources [Tg a<sup>-1</sup>]</b>  | 515±4 <sup>d</sup> | 504±3 <sup>d</sup> | 551±2 <sup>d</sup> |
| Anthropogenic <sup>a</sup>                | 359                | 333                | 371                |
| Seeps, termites                           | 15                 | 15                 | 16                 |
| Open fires                                | 15                 | 16                 | 16                 |
| Wetlands                                  | 126                | 140                | 148                |
| <b>Total sinks [Tg a<sup>-1</sup>]</b>    | 494±4 <sup>e</sup> | 478±3 <sup>e</sup> | 528±2 <sup>e</sup> |
| Tropospheric OH <sup>b</sup>              | 421                | 406                | 455                |
| Other losses <sup>c</sup>                 | 73                 | 72                 | 73                 |
| <b>Mean imbalance [Tg a<sup>-1</sup>]</b> | 21                 | 26                 | 23                 |

910 <sup>a</sup> See Table 1 for sectoral breakdown from the joint inversion.

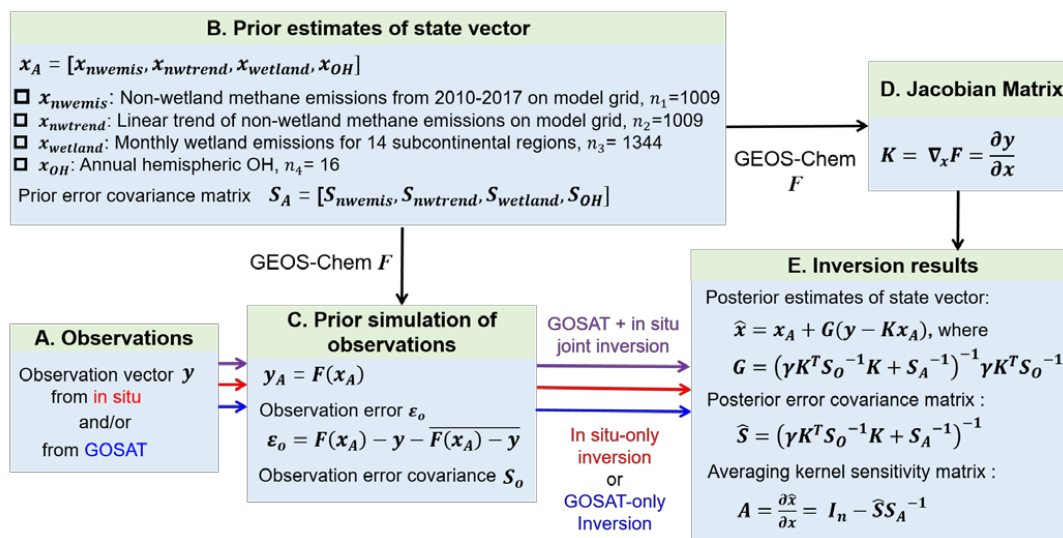
911 <sup>b</sup> Methane lifetime against oxidation by tropospheric OH is 11.2±0.1 years in the GOSAT + in situ inversion.

912 <sup>c</sup> Soils, stratosphere, and oxidation by tropospheric Cl.

913 <sup>d</sup> Error standard deviation estimated from the quadrature of error variance of non-wetland emissions and wetland  
914 emissions.

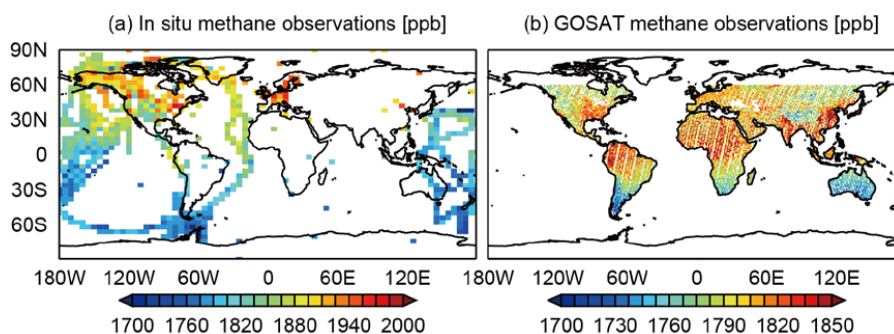
915 <sup>e</sup> Error standard deviation only accounts for the uncertainty in oxidation by tropospheric OH.

916



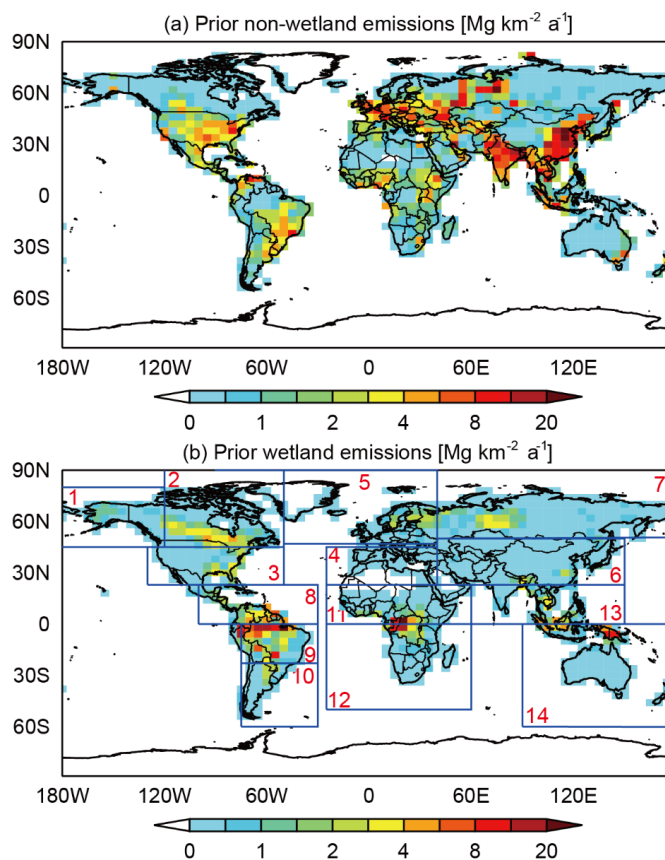
917  
 918  
 919  
 920  
 921  
 922  
 923

**Figure 1.** Analytical inversion framework. The inversion is applied to GOSAT and GLOBALVIEWplus in situ observations for 2010-2017. GEOS-Chem is the chemical transport model (CTM) used as forward model for the inversion.  $\gamma$  is a regularization factor in the Bayesian cost function (see text).



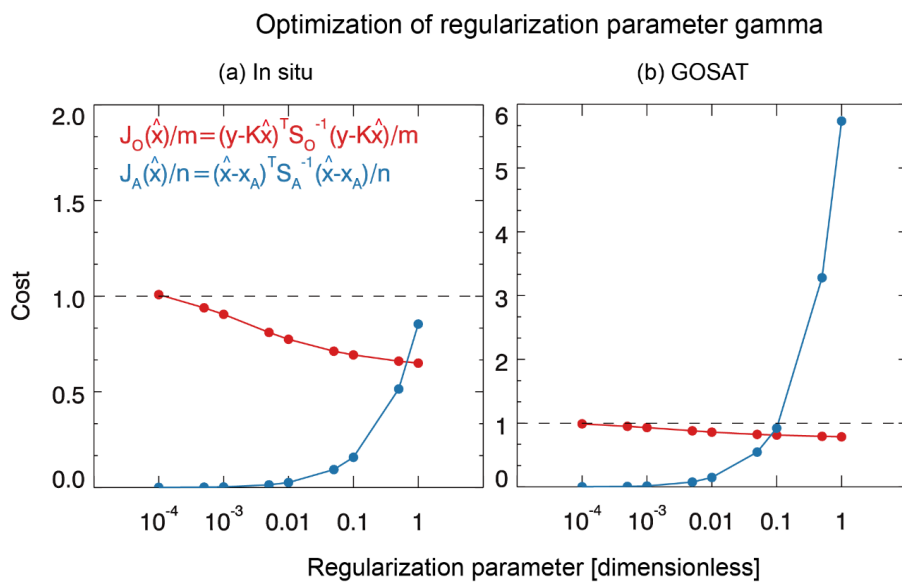
924  
925  
926  
927  
928  
929  
930  
931  
932

**Figure.2** Mean 2010-2017 methane observations from GLOBALVIEWplus ObsPack data product and GOSAT. The GLOBALVIEWplus in situ data are local dry mixing ratios and are averaged over the  $4^{\circ} \times 5^{\circ}$  model grid for visibility. The GOSAT data are dry column mixing ratios on a  $1^{\circ} \times 1^{\circ}$  grid from the University of Leicester version 9 Proxy XCH<sub>4</sub> retrieval (Parker et al., 2020), excluding observations over oceans and poleward of  $60^{\circ}\text{N}$ . Note the difference in color scale between panels.



933

934 **Figure 3.** Prior estimates of mean 2010-2017 methane emissions. The top panel shows the non-wetland  
935 emissions on the  $4^{\circ} \times 5^{\circ}$  grid used for the inversion. The bottom panel shows the wetland emissions and  
936 the 14 subcontinental wetland regions used for the inversion following Bloom et al. (2017).  
937



938

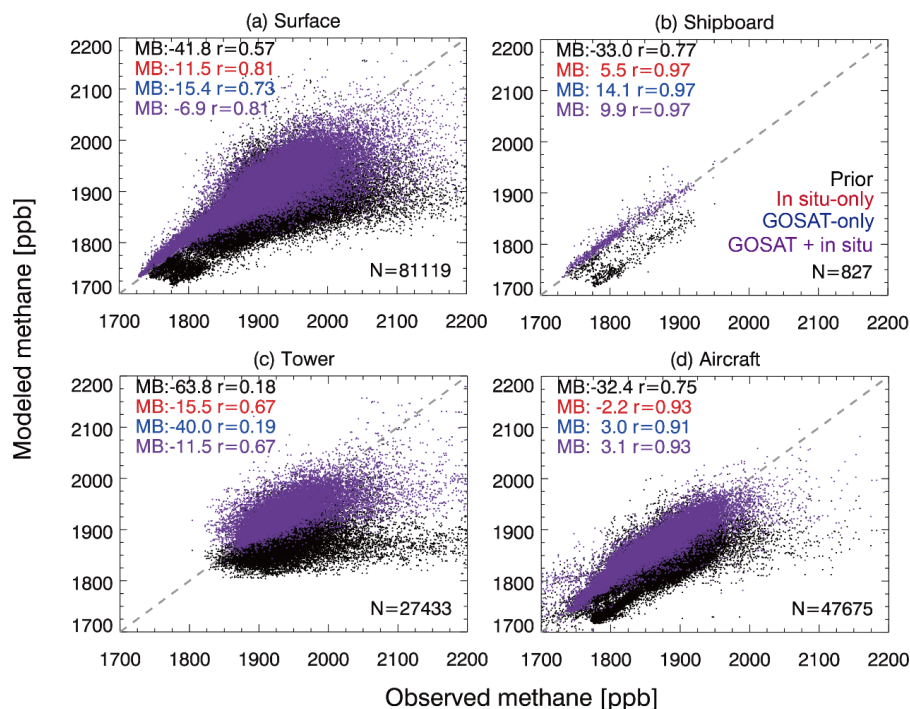
939

940 **Figure 4.** Optimization of the regularization parameter  $\gamma$  in the Bayesian cost function (Equation (1)).

941 The figure shows the posterior observation component  $J_O(\hat{\mathbf{x}}) = (\mathbf{y} - \mathbf{K}\hat{\mathbf{x}})^T \mathbf{S}_O^{-1} (\mathbf{y} - \mathbf{K}\hat{\mathbf{x}})$  and the

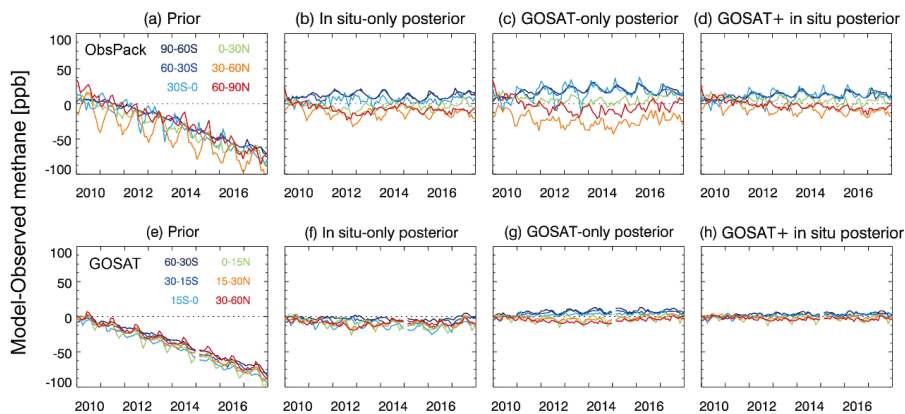
942 posterior state component  $J_A(\hat{\mathbf{x}}) = (\hat{\mathbf{x}} - \mathbf{x}_A)^T \mathbf{S}_A^{-1} (\hat{\mathbf{x}} - \mathbf{x}_A)$  for the In situ-only and GOSAT-only.

943



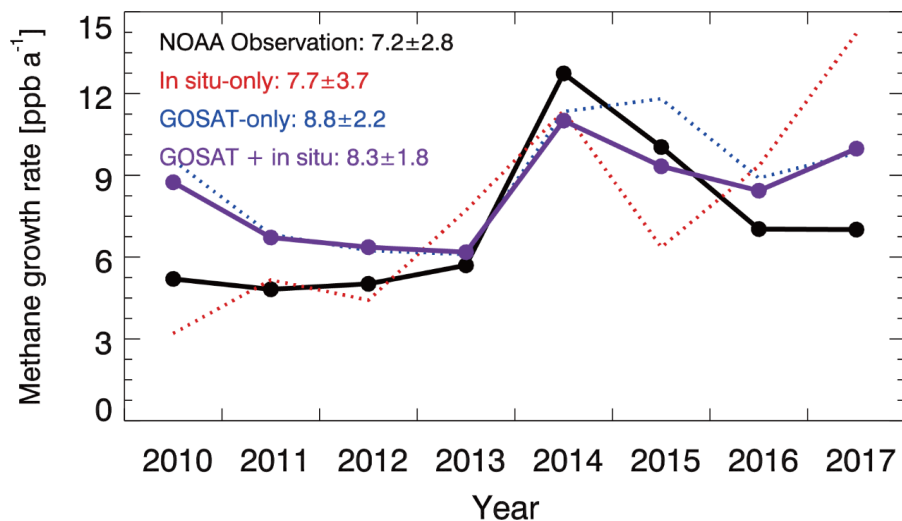
944  
945  
946  
947  
948  
949  
950  
951  
952  
953

**Figure 5.** Ability of the inversions to fit the in situ methane observations. Panels (a)-(d) compare the surface, tower, shipboard, and aircraft observations in 2010-2017 to the GEOS-Chem simulation using the prior (black) and posterior estimates of methane emissions and OH concentrations from the In situ-only inversion (red, dots not shown), GOSAT-only inversion (blue dots not shown), and GOSAT + in situ joint inversion (purple). The numbers (N) of observations from each platform, the mean bias (MB), and the correlation coefficients ( $r$ ) between the observed and simulated values are shown inset.



954  
955  
956  
957  
958  
959  
960  
961

**Figure 6.** Ability of the inversions to fit the in situ methane observations and GOSAT satellite observations. Panels (a)-(d) show the monthly time series of the differences between observed and simulated in situ methane concentrations averaged over different latitude bands from 2010 to 2017. Panels (e)-(h) are the same as panels (a)-(d) but for GOSAT methane concentrations.

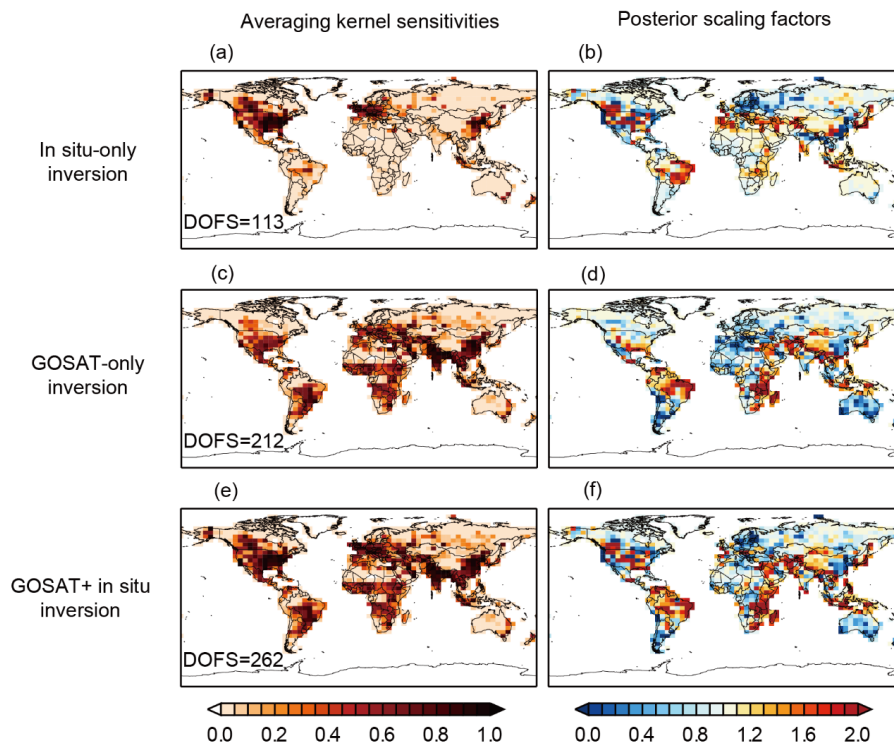


962  
963  
964  
965  
966  
967  
968  
969

**Figure 7.** Annual global growth rate of atmospheric methane, 2010-2017. Results from our three different inversions (In situ-only, GOSAT-only, GOSAT + in situ) are compared to the observed growth rates inferred from the NOAA surface observational network ([https://www.esrl.noaa.gov/gmd/ccgg/trends\\_ch4/](https://www.esrl.noaa.gov/gmd/ccgg/trends_ch4/), last access: 20 June, 2020). Mean annual growth rates and standard deviations from the different inversions are shown inset.



970



971

972

973

974

975

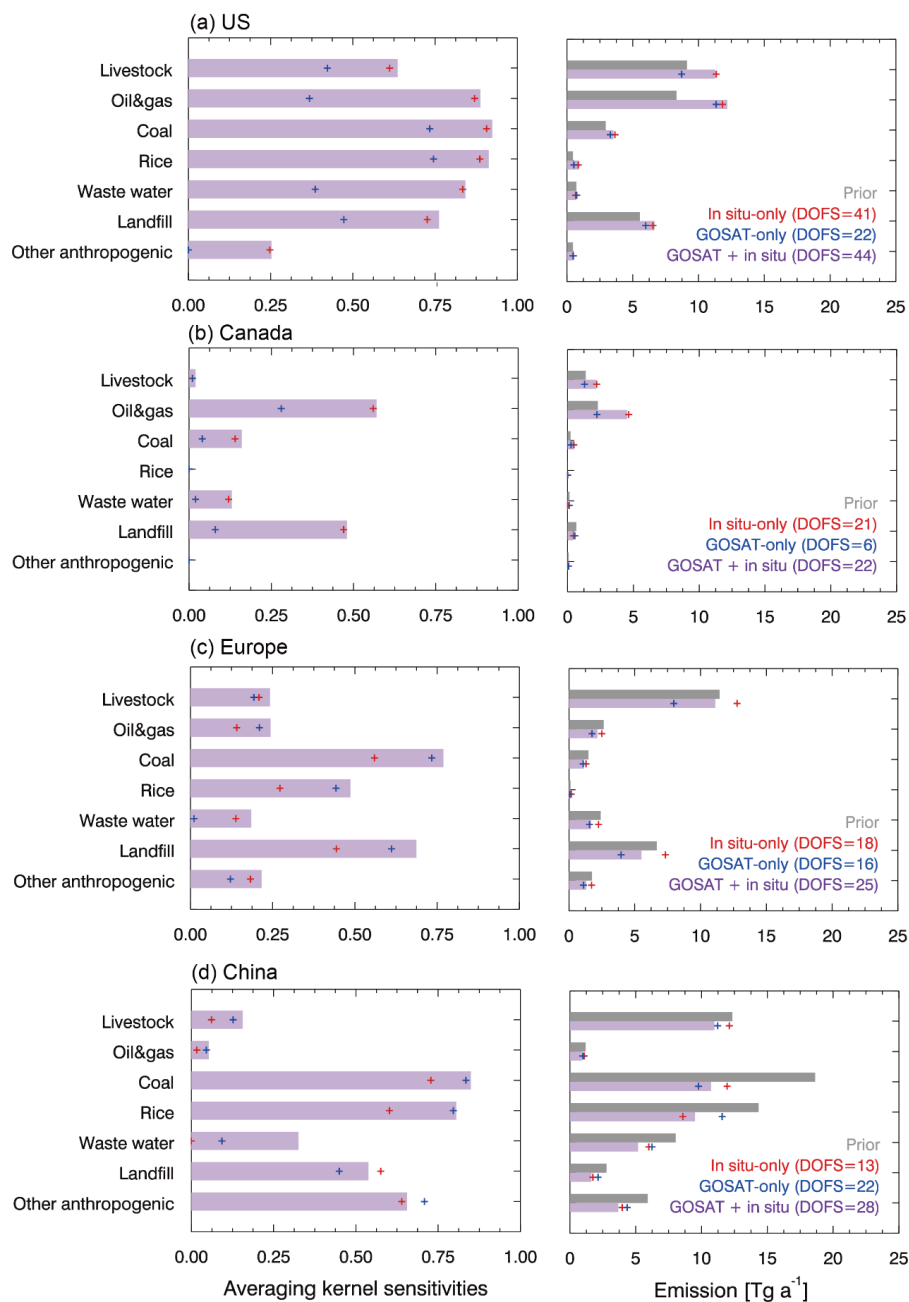
976

977

978

979

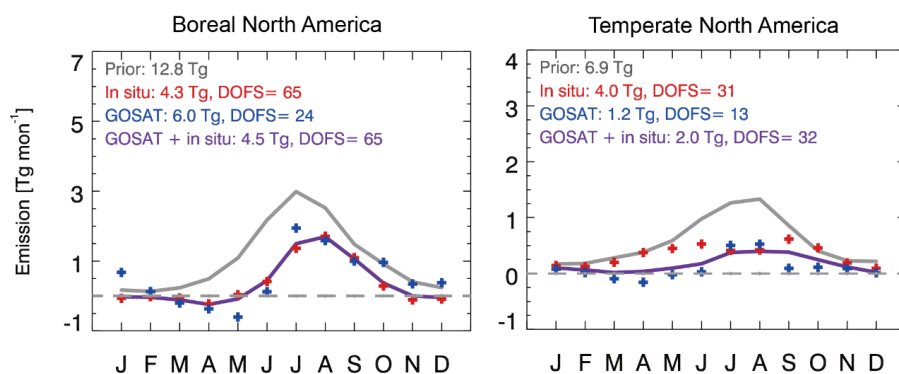
**Figure 8.** Optimization of mean 2010-2017 non-wetland (mainly anthropogenic) emissions. The In situ-only inversion uses in situ observations, the GOSAT-only inversion uses GOSAT satellite observations, and the GOSAT + in situ inversion uses both. The left panels show the averaging kernel sensitivities (diagonal elements of the averaging kernel matrix) for each inversion, with the degrees of freedom for signal (DOFS, defined as the trace of the averaging kernel matrix) given inset. The right panels show the correction factors to the prior emissions (Figure 3a). Wetland emissions are corrected separately (see text).



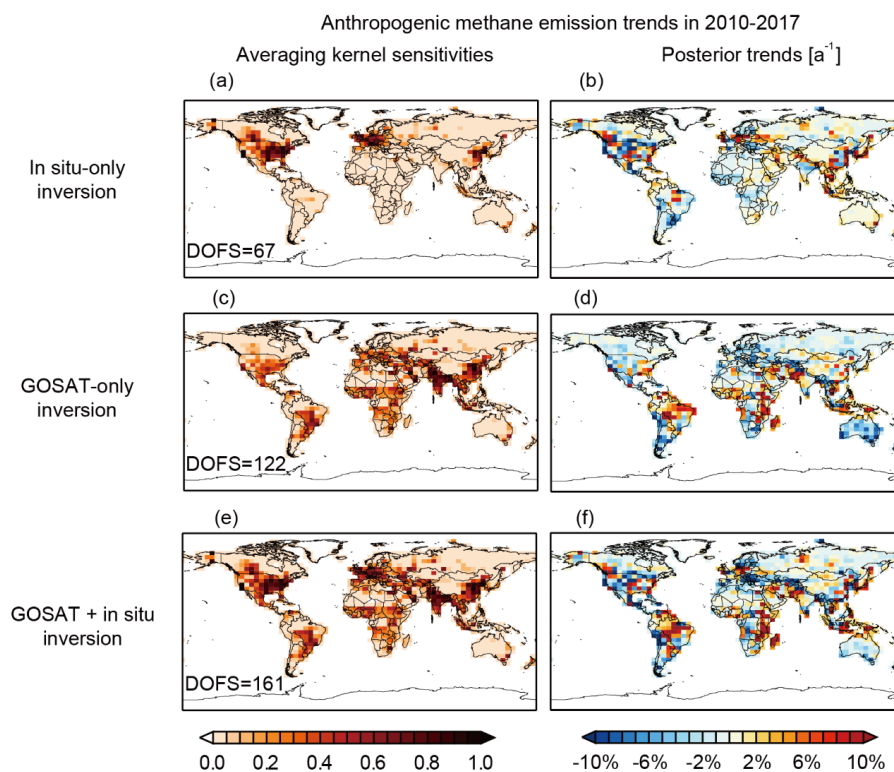
980

981 **Figure 9.** Optimization of anthropogenic methane emissions by source sectors in the In situ-only, GOSAT-  
 982 only, and GOSAT + in situ inversions. The left panel shows the averaging kernel sensitivities for each  
 983 emission sector (see text for description), the right panel shows the emissions. Europe is defined as west  
 984 of 30°E, which excludes Russia.

985

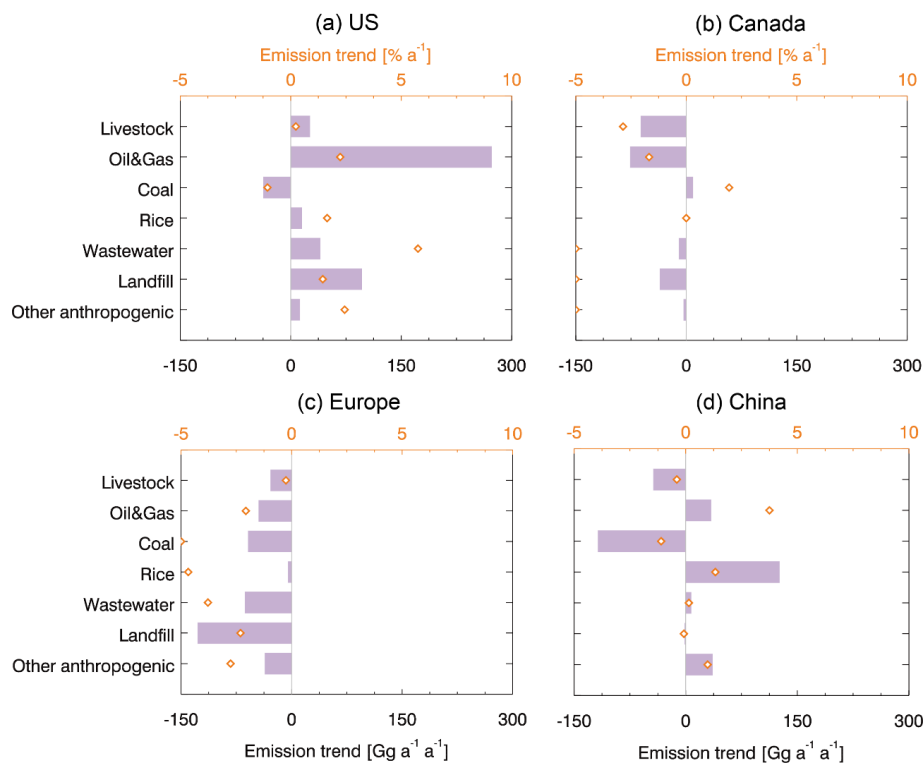


986  
987 **Figure 10.** Wetland emissions in boreal and temperate North America (regions 2 and 3 of Figure 3). Prior  
988 and posterior estimates of the monthly mean wetland emissions averaged over 2010-2017 from different  
989 inversions are shown. Annual mean emissions and the degree of freedom for signal (DOFS) are shown  
990 inset. Note differences in scale between panels. Negative emissions are allowed statistically by the  
991 inversion but are likely not physical.  
992



993  
994  
995  
996  
997

**Figure 11.** Same as Figure 8 but for optimization of non-wetland (mainly anthropogenic) emission trends in 2010-2017.



998

999

1000

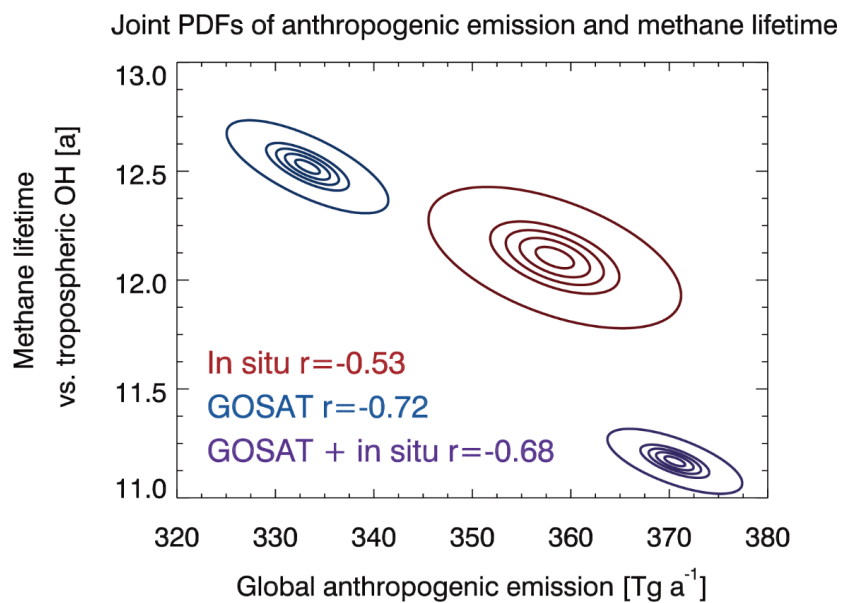
1001

1002

**Figure 12.** Optimization by sector of regional anthropogenic methane emission trends in 2010-2017. Bars and diamonds represent trends in  $\text{Gg a}^{-1} \text{ a}^{-1}$  (bottom axis) and  $\% \text{ a}^{-1}$  (top axis) over the 2010-2017 period from the GOSAT + in situ joint inversion.



1003



1004

1005 **Figure 13.** Joint probability density functions (PDFs) of global mean anthropogenic methane emission  
1006 and methane lifetime against oxidation by tropospheric OH optimized by the three inversions. The thick  
1007 contours show probabilities of 0.99 (outermost), 0.7, 0.5, 0.3, and 0.1 (innermost) from the three base  
1008 inversions. The error correlation coefficients are given inset.

1009

1010

1011

1012